

**H-D inter-diffusion in wadsleyite and ringwoodite:  
Implications for water content and distribution in the  
mantle transition zone**

**2016, March**

**Wei Sun**

**(Doctor Course)**

**The Graduate School of Natural Science and Technology**

**Okayama University**

**H-D inter-diffusion in wadsleyite and ringwoodite:  
Implications for water content and distribution in the  
mantle transition zone**



**Name: Wei Sun**

**Supervisor: Takashi Yoshino**

**Okayama University**

## **Abstract**

Water plays an important role in the Earth's interior, such as triggering the volcanism and seismicity, enhancing plastic deformation and electrical conductivity, and reducing melting temperature and seismic velocities. Especially the mantle transition zone has considered to be a large water budget in the Earth's interior, because wadsleyite and ringwoodite, which are the major phases forming the transition zone, can contain considerable amount of water in their crystal structure. To understand the water distribution and its absolute content, laboratory-based electrical conductivity measurement of wadsleyite and ringwoodite under the condition relevant to the mantle transition zone is a useful method when the data are compared with the conductivity structure determined from electromagnetic surveys. However, the direct conductivity measurements provided large discrepancies among laboratories because of experimental difficulty.

In this study, proton conduction mechanism in wadsleyite and ringwoodite was investigated by high-pressure experiment of H-D inter-diffusion in H- and D-doped single crystal pair to constrain the electrical conductivity of hydrous wadsleyite and ringwoodite. H-D inter-diffusion coefficients were determined at various temperatures between 1000 and 1300 K and pressures of 16 and 21 GPa for wadsleyite with various Mg# and ringwoodite, respectively. To produce hydrogen self-diffusion data with high accuracy, H- and D-doped single crystals of wadsleyite and ringwoodite were synthesized at 16 and 21 GPa, respectively, by slow cooling method. H-D

inter-diffusion experiments of ringwoodite were performed using the H- and D-doped single crystal pair with arbitrary crystallographic direction. H-D inter-diffusion experiments of wadsleyite with various Mg# for three principal crystallographic directions were conducted to investigate the effect of concentration and speciation of hydrogen on inter-diffusion in response to variation of Fe concentration. Diffusion profiles were obtained by secondary ion mass spectroscopy (SIMS).

H-D inter-diffusion profiles in both Fe-bearing wadsleyite and ringwoodite crystal pairs show a symmetrical shape across the interface. Hydrogen self-diffusivities of Fe-bearing wadsleyite and ringwoodite are determined to be  $D_H = 10^{-7.15 \pm 0.46} * \exp(-\frac{106 \pm 11 \text{ kJ/mol}}{2.303 * RT}) \text{ m}^2/\text{s}$  and  $D_H = 10^{-7.29 \pm 0.46} * \exp(-\frac{101 \pm 10 \text{ kJ/mol}}{2.303 * RT}) \text{ m}^2/\text{s}$ , respectively. The hydrogen self-diffusion coefficients of both phases are almost the same and about 1 order of magnitude higher than that of olivine determined at 2 GPa from *Du Frane and Tyburczy* [2012]. There is small anisotropy of hydrogen self-diffusion in Fe-bearing wadsleyite at the mantle transition zone condition.

In Fe-free wadsleyite, inter-diffusion profiles characterized by slower diffusion rate and asymmetry in shape indicate a considerable difference of diffusion coefficients and proton migration mechanism between hydrogen and deuterium in Fe-free condition. Deuterium diffusion coefficient in Fe-free wadsleyite has the same anisotropy and about 1 order of magnitude larger than hydrogen diffusion coefficient. The multiple hydrogen model indicates that the dominant hydrogen migration mechanism changes from Mg sites at the condition with high partially-filled defect concentration to interstitial sites at the conditions with low unfilled defect concentration, and jump

probabilities from Mg sites to interstitial sites between deuterium and hydrogen are different.

Based on the Nernst-Einstein relation, electrical conductivities calculated from the present data of hydrogen self-diffusivities in Fe-bearing wadsleyite and ringwoodite are consistent well with those of *Yoshino et al.* [2008] at the transition zone condition except for ringwoodite at high water content, but are about 1-2 orders of magnitude lower than *Dai et al.* [2009] and *Huang et al.* [2005]. The discrepancies between the conductivity measurements and this study would attribute to varying degrees of dehydration during heating and difference of grain sizes. Compared to the global average one dimensional conductivity-depth model, water concentration in the mantle transition zone is estimated to be less than 1000 ppmw. In the wedge mantle where the subducted slab stagnates, only hydration of wadsleyite and ringwoodite cannot explain both high conductivity and seismic velocity anomalies in subduction slabs. The supercritical fluids generated by heating at the top of subducted stagnant slab would be most possible explanation for both high conductivity and seismic velocity anomalies in the wedge mantle. The characteristic distance for hydrogen self-diffusion in the mantle transition zone is estimated to be  $\sim 1.8$  km after 100 Myr. The heterogeneity of water distribution in the mantle transition zone detected by geophysics observation could be maintained for geologically long time scale. The supercritical fluids long-term preserved in the top of subducted stagnant slab might be most possible explanation for both high conductivity and seismic velocity anomalies in the wedge mantle.

## Contents

<b>Chapter 1: Introduction to mantle mineralogy and hydrogen diffusion</b> .....	8
<b>Chapter 2: Experiments and analysis of synthesis and diffusion</b> .....	20
<b>2.1 Synthesis of hydrous single crystal</b> .....	20
<b>2.2 Analysis of single crystals</b> .....	23
2.2.1 Determination of water content by SIMS.....	24
2.2.2 Determination of water content by FTIR.....	24
2.2.3 Determination of Fe concentration by EPMA.....	27
<b>2.3 H-D exchange experiments</b> .....	27
2.3.1 Determination of typical orientations of wadsleyite single crystals.....	27
2.3.2 H-D inter-diffusion experiments.....	28
2.3.3 SIMS measurements.....	30
<b>Chapter 3: Results of H-D inter-diffusion in wadsleyite and ringwoodite</b> .....	36
<b>3.1 H-D inter-diffusion in Fe-bearing ringwoodite</b> .....	36
<b>3.2 H-D inter-diffusion in Fe-bearing wadsleyite</b> .....	37
3.2.1 H-D inter-diffusion in wadsleyite with high Fe content (Mg#90).....	37
3.2.2 H-D inter-diffusion in wadsleyite with low Fe content (Mg#95).....	39
<b>3.3 H-D inter-diffusion in Fe-free wadsleyite</b> .....	39
<b>Chapter 4: Discussions and implications</b> .....	54
<b>4.1 Hydrogen diffusion mechanism</b> .....	54
4.1.1 Hydrogen migration along interstitial sites.....	54

4.1.2 Evolution of asymmetry in Fe-free condition.....	55
4.1.3 Comparison with <i>Karato (2013)</i> 's model.....	59
<b>4.2 Implication to water distribution in the transition zone.....</b>	<b>61</b>
4.2.1 Bulk hydrogen diffusivities in the transition zone.....	61
4.2.2 Water heterogeneity in the transition zone.....	62
4.2.3 Long-term preserved supercritical fluid in wedge mantle.....	64
<b>4.3 Implications for electrical conduction.....</b>	<b>65</b>
4.3.1 Electrical conductivity in Fe-bearing wadsleyite.....	66
4.3.2 Electrical conductivities in Fe-bearing ringwoodite.....	66
4.3.3 Origin of discrepancy of proton conduction data .....	67
4.3.4 Estimation of water content in the transition zone.....	68
<b>Chapter 5: Concluding remarks.....</b>	<b>85</b>
<b>Acknowledgements .....</b>	<b>88</b>
<b>References.....</b>	<b>89</b>

## Chapter 1

### Introduction to mantle mineralogy and hydrogen diffusion

Water plays important roles in geodynamic processes in the Earth's interior. Since existence of water could affect elastic properties, rheology, phase equilibrium, transport properties, and melting behavior [Kepler and Smyth, 2006], knowledge of water content in the Earth's mantle is essential to understand the mantle dynamics. Although the atmosphere and oceans formed by degassing of the Earth's mantle, measurements of the water contents of natural basalts (quenched glasses or melt inclusions trapped in olivine) suggest that considerable amounts of water could still be stored in the mantle.

The widely accepted mineralogical model in the earth mantle is proposed by Ringwood [1962]. Dominant phases in the upper mantle, from 0 to ~410 km depth, are olivine ( $\text{Fo}_{90}$ ), garnet, orthopyroxene and clinopyroxene. As the main upper mantle constituent Olivine contributes ~60 % in volume and natural olivine usually contains ~10 % of fayalite constituent, namely,  $(\text{Mg}_{0.9}\text{Fe}_{0.1})_2\text{SiO}_4$ . The volume fraction of garnet increases with increasing depth accompanied by decrease of proportion of both orthopyroxene and clinopyroxene (**Fig. 1.1**). At the 410-km depth seismic discontinuity, with a pressure of ~14 GPa, and temperature of ~1700 K, olivine transits to its  $\beta$  phase, wadsleyite, furthermore, to  $\gamma$  phase, ringwoodite, at 520 km depth (~18 GPa, 1900 K). The wadsleyite and ringwoodite, with ~40 % of garnet, constitute the transition zone (410-670 km depth) (**Fig. 1.1**). In the lower mantle with

depth >670 km, (Mg,Fe)SiO<sub>3</sub> perovskite and (Mg,Fe)O ferropericlae are stable and constitute the main part of lower mantle.

Main constituent minerals forming most of the mantle contain no water in chemical formula and are referred as nominally anhydrous minerals (NAMs). However, it is well known that NAMs can store significant concentrations of hydrogen as defects in their crystal structures. Although the hydrogen proton (H<sup>+</sup>) can be considered as a monovalent cation, it does not occupy the same structural position as a typical cation in a mineral structure and instead it forms a hydrogen-bond with oxygen on the edge of the coordination polyhedron. Trace amounts of hydrous components can dramatically influence physical properties of minerals; the mechanical strengths and melting temperatures are suppressed [e.g., *Inoue et al.*, 1998; *Liu*, 2002; *Holl et al.*, 2008] whereas the diffusivities and electrical conductivities are enhanced [e.g., *Kohlstedt and Mackwell*, 1998; *Demouchy and Mackwell*, 2003; *Huang et al.*, 2005; *Hae et al.*, 2006; *Yoshino et al.*, 2008]. Understanding the behavior and kinetics of proton defects in olivine and its high pressure polymorphs, wadsleyite and ringwoodite, which are considered as dominant minerals in the Earth's upper mantle and transition zone [*Ringwoodite and Major*, 1970], is thus of a fundamental importance to develop the model of evolution and dynamics of mantle.

To estimate water content and its variation in the mantle, electrical conductivity would be useful because water seems to have a strong influence on electrical conductivity even in a very small amount, and ionic conduction by highly mobile

protons may enhance the electrical conductivity of the mantle rocks [Karato, 1990]. Once the electrical conductivities of the dominant mantle minerals are well defined as a function of water content, we can estimate the water content from the electrical conductivities observed from magneto-telluric (MT) methods.

Electrical conductivity in the mantle has been obtained by magnetotelluric (MT) [Egbert, 2007] and geomagnetic deep sounding (GDS) [Banks, 2007]. Initial pioneering studies were restricted to local areas beneath continents [e.g., Schultz *et al.*, 1993; Olsen, 1999]. Recent studies show that better models of conductivity profiles in the oceanic area can be achieved through use of ocean bottom electromagnetometers [Evans *et al.*, 2005; Seama *et al.*, 2007; Baba *et al.*, 2010]. Semi-global electromagnetic induction studies using a submarine cable across the Pacific have also developed a better reference model [Utada *et al.*, 2003; Kuvshinov *et al.*, 2005; Shimizu *et al.*, 2010]. A three-dimensional electrical conductivity distribution by using a global dataset with improved inversion schemes is currently available down to the uppermost lower mantle [Kelbert *et al.*, 2009]. As a general feature, electrical conductivity of the oceanic upper mantle at ~100 km depth is very high, about  $10^{-2}$  to  $10^{-1}$  S/m. This zone is known in seismology as the high conductive layer, corresponding to the low-velocity zone [e.g., Lizzaralde *et al.*, 1995; Evans *et al.*, 2005; Baba *et al.*, 2010]. Conductivity generally increases with increasing depth to the top of the lower mantle from  $10^{-3}$  –  $10^{-2}$  to  $10^0$  S/m [e.g., Neal *et al.*, 2000; Utada *et al.*, 2003; Tarits *et al.*, 2004; Semenov and Jozwiak, 2006; Kelbert *et al.*, 2009; Shimizu *et al.*, 2010]. It is accepted that local variations of electrical conductivity are

large at shallow depths, but become smaller with increasing depth. However, recent electromagnetic studies have shown a great variety of lateral heterogeneities in conductivity structure of the mantle transition zone [e.g., *Ichiki et al.*, 2001; *Booker et al.*, 2005; *Kelbert et al.*, 2009].

Electrical conductivity of mantle rocks is controlled by not only water content in main constituent minerals but also mineral species and their chemical composition under specific physical conditions, such as pressure, temperature and oxygen fugacity. Therefore, *in situ* laboratory measurements of electrical conductivity of the major mantle phases under high-pressure and high-temperature conditions have been performed. In conjunction with conductivity-depth profiles of the mantle (derived from electromagnetic data), their conductivity measurement have provided some constraints on temperature and chemistry, especially of water content, in the Earth interior [e.g., *Katsura et al.*, 1998; *Xu et al.*, 1998; *Huang et al.*, 2005; *Wang et al.*, 2006; *Yoshino et al.*, 2006; 2008; 2009; *Romano et al.*, 2009; *Dai and Karato*, 2009].

Among the main constituent mantle minerals, wadsleyite and ringwoodite can contain relatively large amount of water (more than 2 wt.%) in their crystal structures [e.g., *Inoue et al.*, 1995; *Kohlstedt et al.*, 1996; *Bolfan-Casanova et al.*, 2000]. Therefore, the mantle transition zone has been considered to be the largest water container in the Earth's interior. Although knowledge of the H<sub>2</sub>O storage capacity, which is defined as the maximum mass fraction of water that can be retained in a rock or mineral at a given temperature and pressure has accumulated, it is difficult to determine actual water content and its distribution from such information alone. Thus,

we need knowledge of the electrical conductivity of mantle minerals as a function of water content to directly determine its content and distribution in the present mantle transition zone from the geophysical data. However, water content in the mantle is still largely unknown.

Many researchers have striven to determine the conductivity of mantle transition zone minerals [*Huang et al.*, 2005; *Yoshino et al.*, 2006; 2008; *Wang et al.*, 2006; *Manthilake et al.*, 2009; *Dai and Karato*, 2009; *Romano et al.*, 2009]. However, there has been large divergence on direct electrical conductivity measurements of hydrous wadsleyite and ringwoodite among former studies, mainly dividing into two groups: (1) Misasa group (*Yoshino et al.* [2008], [2012]; *Manthilake et al.* [2009]) and (2) Yale group (*Dai and Karato* [2009] and *Huang et al.* [2005]). Electrical conductivities of Yale group on hydrous wadsleyite and ringwoodite are ~1 and ~2 orders of magnitude higher than Misasa group in the same conditions, respectively. Recently conductivity-depth profiles down to the mantle transition zone as a function of water content have been put forth, which use the inconsistent conductivity data [*Karato*, 2011; *Khan and Shankland*, 2012; *Jones et al.*, 2012; *Yoshino and Katsura*, 2013]. These suggest water content differences estimated by various databases that are occasionally greater than one order of magnitude.

Direct electrical conductivity measurements on NAMs, at present experiment condition only polycrystals available on wadsleyite and ringwoodite, is quite difficult because of dehydration during long duration of heating, especially at high temperature and high water content. Water incorporated as hydroxyl in the mineral lattice might

escape and trap as supercritical fluid within grain boundary. Electronic current flow might acquire a much fast-path along grain boundary fluid in addition to slow lattice transfer. Former measurements of supercritical water based on shock experiments at 15 GPa and 1273K yielded a conductivity of 100 S/m [Mitchell and Nellis, 1982], which is ~4 orders of magnitude higher than lattice proton conductivity. Even if tiny amount of dehydrated water exists in the measure sample, observed electrical conductivity would be largely overestimated, especially on high water content and fine-grained sample.

To solve origin of disagreements of the conductivity values among labs, estimation from hydrogen self-diffusion coefficient is another devisable method to obtain proton conductivity based on the Nernst-Einstein relation, which is expressed as

$$\sigma_p = \frac{D_H C_H q^2}{kT} \quad (1.1)$$

where  $D_H$  is the hydrogen self-diffusion coefficient,  $C_H$  is concentration of hydrogen,  $q$  is charge,  $k$  is the Boltzmann constant, and  $T$  is absolute temperature. This method can exclude uncertainties of the estimation of proton conduction in the lattice due to dehydration during the conductivity measurement even at high temperatures. It might provide more accurate proton conductivities of wadsleyite and ringwoodite, especially at high water content.

*Hae et al.* [2006] investigated hydrogen diffusivities in synthesized polycrystals Fe-bearing wadsleyite. However, because grain boundary diffusion are usually several orders of magnitude larger than lattice diffusion in polycrystals [Demouchy, 2010], in

the case of fine-grained aggregates, most of hydrogen migrates along grain boundary instead of crystal interior based on the expression proposed by *Balluffi et al.* [2005]

$$D_H^{eff} = D_H^L + \left(\frac{3\delta}{d}\right)D_H^{gb} \quad (1.2)$$

where  $D_H^{eff}$ ,  $D_H^L$  and  $D_H^{gb}$  are hydrogen diffusivities for bulk, lattice and grain boundary, respectively.  $d$  is the grain size and  $\delta$  is the grain boundaries width. Imaging of grain boundaries using transmission electronic microscopy permitted the measurement of grain boundaries widths and to date is considered to be equal to 0.75 nm (two monoatomic layers) [*Hiraga and Kohlstedt, 2007, 2009*]. In *Hae's* study, the grain sizes of wadsleyite polycrystals are  $\sim 9 \mu\text{m}$ . Thus, their result is probably an approximation of hydrogen grain boundary diffusion rather than hydrogen lattice self-diffusion and cannot be applicable to the proton conductivities based on the Nernst-Einstein relation. The estimated water content in the transition zone would be underestimated since grain size in mantle seems to be much larger.

To determine the hydrogen self-diffusion in NAMs accurately, usage of single crystal makes it possible to exclude the effect of grain boundary diffusion. Hydrogen lattice self-diffusion experiments using large single crystals obtained from nature or synthesized crystals, a large number of hydrogen diffusion experiments have been performed on olivine or forsterite [*Kohlstedt and Mackwell, 1998; Demouchy and Mackwell, 2003, 2006; Du Frane and Tyburczy, 2012; Padrón-Navarta et al., 2014*]. However, there has been no lattice self-diffusion experiments conducted on single crystals of wadsleyite and ringwoodite before.

Most of former studies in olivine are benefited from chemical diffusion, where

hydrogen atoms transfer from surrounding wet polycrystals to a center dry single crystal (**Fig. 1.2**). As soon as ferric iron or original vacant in dry crystals consumed, hydrogen chemical diffusion will be stagnated because of charge equilibrium. Hydrogen cannot transfer until new magnesium vacant generate through slower magnesium vacancy diffusion [Demouchy and Mackwell, 2006].

Kohlstedt and Mackwell [1998] identified two mechanisms for hydrogen chemical diffusion: (1) a faster “redox exchange” mechanism ( $D_{redox}$ ) and (2) a slower “incorporation” mechanism ( $D_{incorp}$ ). Redox exchange involves exchange of hydrogen with charged polarons, electron holes (h) created by a ferric iron ion on an octahedral site  $Fe_{Me}^{\cdot}$ .  $D_{redox}$  can be expressed as

$$D_{redox} = \frac{(X_h + X_H)D_h D_H}{X_h D_h + X_H D_H} \quad (1.3)$$

where  $D_H$  is the hydrogen self diffusivity,  $X_H$  is the concentration of hydrogen,  $D_h$  is the diffusivity, and  $X_h$  is the concentration of small polaron. For the special case  $X_H = X_h$  and if  $D_h \gg D_H$  then it follows that  $D_{redox} \approx 2D_H$ . The slower hydrogen incorporation mechanism involves a simultaneous flow of metal vacancies ( $V_{Me}''$ ), with chemical diffusivity expressed as

$$D_{incorp} = \frac{3D_V D_H}{2D_V + D_H} \quad (1.4)$$

where  $D_V$  represents the hydrogen diffusivity through metal vacancies. If  $D_H \gg D_V$ , then it follows that  $D_{incorp} \approx 3D_V$ .

However, ferric iron or original vacancy consumes within a short duration and dissipation points are impossible to determine during practical diffusion experiments. The redox diffusivities are usually affected by incorporation mechanism and thus

hydrogen chemical diffusion experiments prefer to deduce impure hydrogen self-diffusion coefficients.

Isotopic inter-diffusion is a process occurring in a system with difference in the isotopic ratio of the same element, but no chemical potential gradient in terms of elemental composition. Therefore, the external driving forces such as gradients of chemical potential and/or electrical potential are equal to zero in a self-diffusion process. Jumping of atoms is followed by a random walk. The diffusion coefficient of an isotope of a given atomic species is often referred to as the self-diffusion coefficient of the atom. Because the isotopes of a given species have exactly the same electronic charge, their chemical bonds are identical. Consequently, when a gradient in the concentration of one isotope is present, the motion of the isotope through the matrix does not cause any changes in energy, and there is no interaction between isotopes.

*Du Frane and Tyburczy* [2012] introduced the H-D exchange method to determine hydrogen self-diffusion coefficients in olivine because this method has an advantage to distinguish between incorporation and self-diffusion, and provides more accurate hydrogen self-diffusion coefficients attributing to proton conduction than traditional incorporation method [*Kohlstedt and Mackwell*, 1998; *Demouchy and Mackwell*, 2003; *Hae et al.*, 2006]. The H-D inter-diffusion coefficient ( $D_{H-D}$ ) obtained from the diffusion profile depends on the concentrations of D and H:

$$D_{H-D} = \frac{(X_D + X_H)D_D D_H}{X_D D_D + X_H D_H} \quad (1.5)$$

where  $D_H$  and  $D_D$  are the self-diffusivity of hydrogen and deuterium, respectively,

and  $X_H$  and  $X_D$  are concentration of hydrogen and deuterium, respectively.  $D_{H-D}$  varies in value between  $D_H$  and  $D_D$  depending on both time and distance from the edge of the crystal, which contacts with the other isotope-doped crystal. Because absolute rate theory predicts only a small difference between diffusivity of D and H due to the similar mean thermal velocity, with  $D_D = \sqrt{2}D_H$ , the H-D inter-diffusion coefficient is a good approximation of hydrogen self-diffusion.

However, *Du Frane's* experiments are not defined as H-D inter-diffusion since they did not use both H- and D-doped single crystals (**Fig. 1.2**) and thus would introduce some impurity component from water incorporation and grain boundary diffusions. In addition, huge concentration difference between H-doped single crystal and surrounding D-doped polycrystals could lead to chemical diffusion in their runs, and the diffusion profile obtained from H-doped single crystal was not derived from a single line across the interface between D-doped surrounding crystals and H-doped single crystal. Thus the determined diffusion coefficient would contain large errors.

To produce hydrogen self-diffusion data with a high accuracy, in this work, we employed H- and D-doped single crystal diffusion couples of wadsleyite and ringwoodite, which were synthesized at 16 and 21 GPa, respectively, through slow cooling method. H-D inter-diffusion experiments for wadsleyite with various Mg# and ringwoodite with constant Mg# (90) were performed in multi-anvil at various temperatures between 1000 and 1300 K and pressures as same as synthesis. As for wadsleyite, paralleled H-D inter-diffusion experiments were conducted with various Mg# to constrain variations of concentration and speciation of migrate hydrogen

during inter-diffusion in response to Fe content. Diffusion profile analysis was performed by Secondary ion mass spectroscopy (SIMS). Temperature dependences of hydrogen diffusivities were determined based on the Arrhenius equation. The main aims of this study were:

- (1) Determining the pre-exponential factors  $D_0$  ( $\text{m}^2/\text{s}$ ) and the activation enthalpies  $H_a$  (kJ/mol) for hydrogen isotopes self-diffusion in wadsleyite and ringwoodite at 16 and 21 GPa, respectively.
- (2) Determining anisotropies of hydrogen isotopes diffusion in Fe-bearing and Fe-free wadsleyite.
- (3) Investigating concentration and speciation of mobile hydrogen during inter-diffusion with various Fe concentrations in wadsleyite at 16 GPa.
- (4) Constraining water distribution in mantle transition zone by calculation of hydrogen characteristic diffusion distance in Fe-bearing wadsleyite.
- (5) Expecting electrical conductivities from present hydrogen self-diffusivities in Fe-bearing wadsleyite and ringwoodite based on Nernst-Einstein equation and comparing with former direct conductivity measurements to explain large discrepancies on the former studies among laboratories.
- (6) Constraining water content in the mantle transition zone and providing the most plausible explanation for both high conductivity and fast seismic velocity anomalies in the wedge mantle.

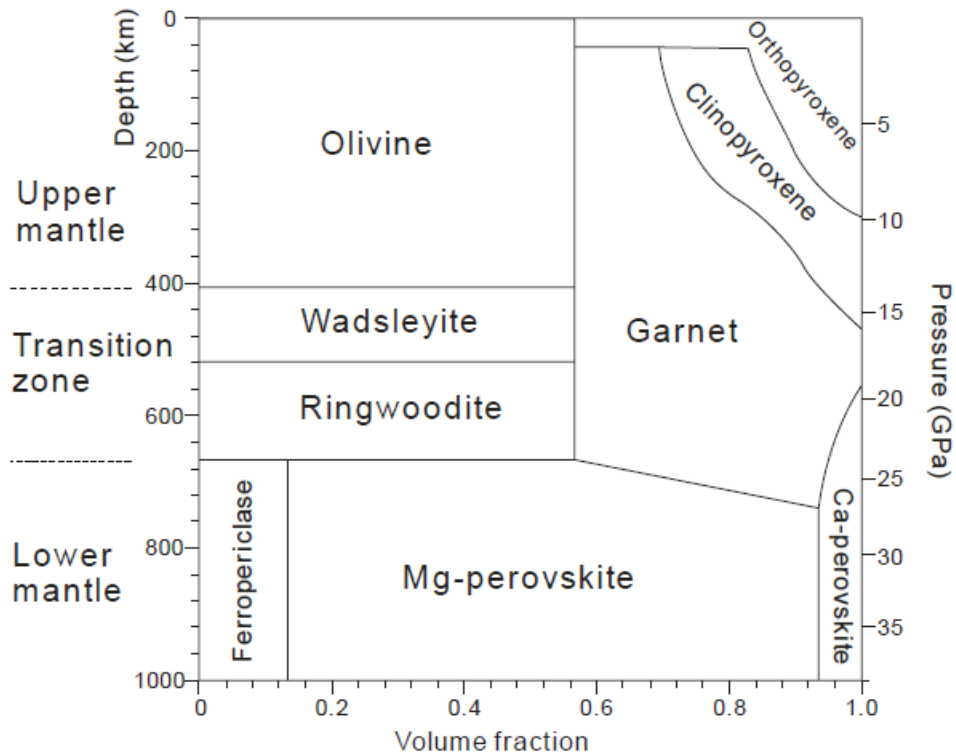


**Fig. 1.1.** Mineralogical model of the Earth's mantle (modified from *Shekhar* [2012]).

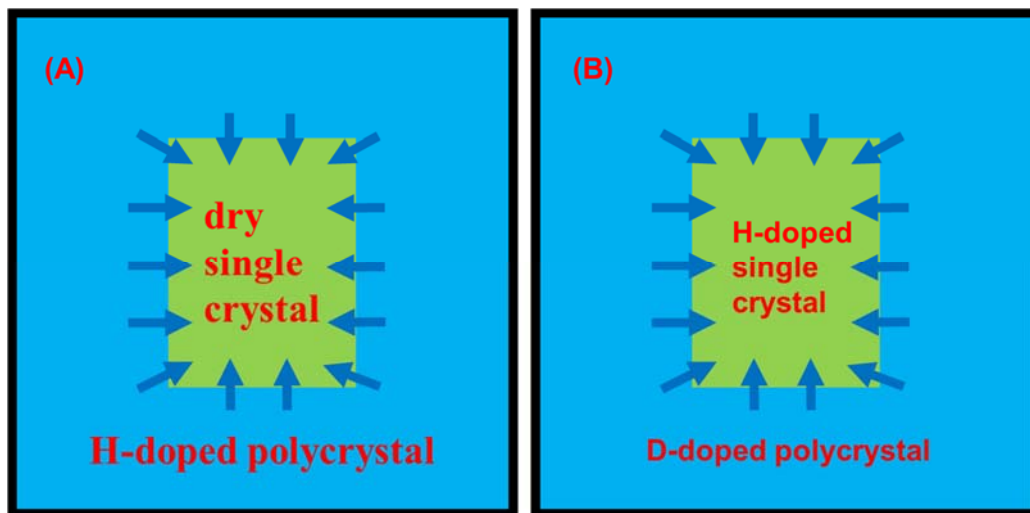


**Fig. 1.2.** assembly examples from former hydrogen diffusion studies for (A) chemical diffusion experiments [*Kohlstedt and Mackwell*, 1998; *Demouchy and Mackwell*, 2003, 2006; *Hae et al.*, 2006] (B) H-D exchange experiments [*Dufrane and Tyburczy*, 2012].

## Chapter 2

### Experiments and analysis of synthesis and diffusion

#### 2.1 Synthesis of hydrous single crystal

To synthesize large single crystals of high-pressure minerals, there are generally two methods: one is thermal gradient method [Shatskiy *et al.*, 2009] and another is slow cooling method [Shatskiy *et al.*, 2010]. Shatskiy *et al.* [2009] has synthesized large single crystals of hydrous wadsleyite crystallized from  $K_2Mg(CO_3)_2 \cdot H_2O$  (KMC) solvent. However, there are two drawbacks to this solvent: (1) water solubility of crystals growth from carbonate melt is lower than that synthesized from pure water [Litasov and Ohtani, 2009]. For example, ~4000 ppmw water is one-third of water solubility in wadsleyite coexisting with hydrous melt. Low water fugacity condition, where wadsleyite crystals were synthesized from carbonate solvent, can lead to low water solubility. (2) Carbonate inclusions are likely to appear in wadsleyite crystals especially for large ones. A presence of the inclusions reduces the quality of single crystals. However, carbonate solvent could be the only option for thermal gradient method since attempts of synthesis of large wadsleyite crystals (>1 mm) from water solvent were failed by previous studies [Shatskiy *et al.*, 2009; Jacobsen *et al.*, 2005; Nishihara *et al.*, 2006]. Although slow cooling method could synthesize larger crystals than thermal gradient method, compositional heterogeneity always appears as a considerable problem for H-doped or Fe-bearing crystals because of wide variations of water solubility and Fe partition coefficient from melt as temperature decreases

[Demouchy *et al.*, 2005].

The synthesis experiments were conducted in either 1000 or 5000 ton Kawai-type multi-anvil apparatus in the Institute for Study of the Earth's Interior, Okayama University. Cr-doped MgO octahedron with edge lengths of 14 and 10 mm and tungsten carbide cubes with truncation edge lengths of 6 and 5 mm were used for synthesis of wadsleyite and ringwoodite, respectively.

First trial to synthesize H- and D-doped wadsleyite crystals is based on thermal gradient method developed by Shatskiy *et al.* [2009]. A mixture of  $K_2CO_3$ ,  $MgCO_3$  and  $Mg(OH)_2$  (or  $Mg(OD)_2$ ) with 14 wt.% bulk water content was used as solvent. The sealed Pt capsule (2.5 mm in length and diameter) surrounded by MgO was loaded in a stepped  $LaCrO_3$  cylindrical heater and the center of the capsule was shifted 0.6 mm from the center of the heater along the axial direction so that the silicate source and solvent were placed in the hot and cool regions respectively to create a monotonic thermal gradient in the axial direction (**Fig. 2.1**).  $W_{97}Re_3$ - $W_{75}Re_{25}$  thermocouple was placed at the hotter side. The ratio of thin and thick parts for stepped heater is 2:3 and test experiment with double thermocouples revealed the thermal gradient of our assemblies was around 30 °C /mm at 1673 K and 16 GPa.

Several experiments were conducted at 1400 °C and 16 GPa. However, most of large crystals grown from KMC solvent contained a lot of carbonate inclusion with white color and only some small crystals are inclusion-free. Therefore, the solvent was changed to pure water. The recovered crystals are less than 500  $\mu m$  although they are free of inclusion, suggesting low solubility of  $Mg_2SiO_4$  in supercritical fluids

rather than carbonate solvent at the synthetic condition. However, the crystal size is not enough to use for the diffusion experiment.

Next, the slow cooling method (gradual crystallization from silicate partial melts) was applied to obtain larger single crystals. In addition to conventional slow cooling method (ref.), the sample was kept at the final target temperature for more than 2 hours after cooling to homogenize the water and iron contents in single crystals because water solubility in wadsleyite and ringwoodite is sensitive to temperature [Litasov *et al.*, 2011]. Therefore, it is necessary to be kept at high temperature below the melting temperature for more than 2 hours to homogenize the water content in the single crystals after slow cooling. As a consequence, large single crystals of H- and D-doped wadsleyite with different Fe content were successfully synthesized by this method: (1) Fe-free wadsleyite (2) Fe-bearing wadsleyite with Fo<sub>95</sub> composition (3) Fe-bearing wadsleyite with Fo<sub>90</sub> composition, respectively.

For Fe-free wadsleyite, the starting silicate source was powder (< 1  $\mu\text{m}$ ) of forsterite smashed from single crystals, which was packed and occupied 2/3 of a Pt capsule, and the remaining part is filled with solvent composed of oxide mixture Mg(OH)<sub>2</sub> or Mg(OD)<sub>2</sub> + SiO<sub>2</sub> + MgO (18 wt.% H<sub>2</sub>O or D<sub>2</sub>O). To minimize water loss, the Pt capsule was welded in liquid nitrogen. The design of cell assembly is same as the thermal gradient method. After heating to the maximum temperature higher than melting temperature of water-saturated wadsleyite, temperature was slowly decreased from 2073 to 1723 K with cooling rate of 1 K/min and then kept at 1723 K for > 2 hours before quench.

For Fe-bearing wadsleyite, silicate source is powder ( $< 1 \mu\text{m}$ ) of natural San Carlos olivine and the solvent composed of oxide mixture  $\text{Mg}(\text{OH})_2$  or  $\text{Mg}(\text{OD})_2 + \text{SiO}_2 + \text{MgO} + \text{FeO}$  ( $\text{Mg}\# = 85$  and  $10 \text{ wt.}\% \text{ H}_2\text{O}$  or  $\text{D}_2\text{O}$ ). Two types of capsule material (Pt and Au) were used to implement different Fe and  $\text{Fe}^{3+}$  content. The wadsleyite sealed in Pt capsules showed Fe loss to capsules after recovery, while the starting Fe composition was kept well in Au capsules. Because melting temperature of Au is lower than that of Pt, the slow cooling in Au capsules were conducted from 1923 to 1723 K with cooling rate of  $1 \text{ }^\circ\text{C} / \text{min}$ . In addition, duration of annealing at 1723 K increased to  $>5$  hours for Fe-bearing wadsleyite because of lower mobility of Fe than H [Li *et al.*, 2015].

For Fe-bearing ringwoodite, the starting silicate source and solvent are completely same as Fe-bearing wadsleyite. Because it is relatively difficult to place a stepped heater in the 10 mm MgO octahedron, only a straight  $\text{LaCrO}_3$  cylindrical heater was used to synthesize large single crystals of H- and D-doped Fe-bearing ringwoodite. Au capsule (2.5 mm in length and diameter) was used for sealing. Slow cooling was conducted from 2023 to 1723 K with cooling rate of  $1 \text{ }^\circ\text{C} / \text{min}$  and then temperature was kept at 1723 K for  $> 5$  hours at 21 GPa.

## 2.2 Analysis of single crystals

The largest grain size of synthesized Fe-free wadsleyite, Fe-bearing wadsleyite and ringwoodite are  $\sim 1.2$ , 1.8 and 1.8 mm, respectively (**Fig. 2.2**). Most of single crystals are in good quantity, transparent and free of inclusion. Homogeneity of

H<sub>2</sub>O(D<sub>2</sub>O) contents in single crystals were confirmed by using both Secondary ion mass spectroscopy (SIMS) and Fourier-transformed infrared (FTIR) spectroscopy. Homogeneity of Fe content in Fe-bearing crystals were confirmed by Electron probe micro-analyzer (EPMA) (Table 2.2).

### 2.2.1 Determination of water content by SIMS

Water contents in synthesized single crystals were measured by secondary ion mass spectroscopy (SIMS), Cameca 6F and 1270 at Hokkaido University. The polished crystals were coated with Au layer of ~30 nm by plasma sputtering. A primary Cs<sup>+</sup> ion beam operated at 17-20 nA, and was focused to form a large crater with 100 μm diameter on the sample, and the secondary <sup>1</sup>H-, <sup>2</sup>H- and <sup>30</sup>Si- ions were collected from the center region of the sputtered area using a large mechanical aperture to minimize background arising from hydrogen adsorbed on the polished surface. A normal incident electron flood gun was used for charge compensation. The entrance and exit slits were narrowed enough to minimize the contribution of <sup>28</sup>Si<sup>2</sup>H- to <sup>30</sup>Si. Hydrogen and deuterium content of single crystals were calculated from ions counts ratio of <sup>1</sup>H-(<sup>2</sup>H-)/<sup>30</sup>Si- multiplied by a correlation coefficient (unpublished data from *Tomioka*).

$$c_{OH(OD)} \text{ in wt. \%} = 0.68753 \times R_{H(D)/Si} \quad (2.1)$$

### 2.2.2 Determination of water content by FTIR

To quantify the water content in ppm weight, unpolarized infrared absorption spectra of synthesized wadsleyite single crystals were inspected using JASCO MFT-2000 Fourier transform infrared spectrometer (FTIR) in the Institute for Study

of the Earth's Interior, Okayama University. Measurements were carried out using a Ge coated KBr beam splitter and a high-sensitivity wide band MCT (Mercury–Cadmium–Telluride) detector cooled by liquid N<sub>2</sub>, with a 4 cm<sup>-1</sup> resolution in air. The synthetic single crystal was double-polished to a thickness of 20–80 μm. This crystal thin sections with arbitrary orientations were put on a KBr plate. The aperture size of 30× 30 μm (50×50 μm, in some cases) was adopted to obtain infrared absorption spectra.

IR spectra were obtained from more than 2 points in several large crystals synthesized from a single run. Due to unavoidable contamination of H<sub>2</sub>O from air before capsule welding, D-doped crystals contained significant amount of H. Total water content (H<sub>2</sub>O + D<sub>2</sub>O) is not always same between H- and D-doped single crystal pairs although the synthesis conditions were completely same. Water content in wadsleyite were calculated based on the equation developed from *Paterson et al.* [1982] and consistent quality with SIMS measurements.

There has been no theoretical equation from unpolarized FTIR spectra to calculate either OH or OD concentration in wadsleyite and ringwoodite before. *Paterson* [1982] has proposed a classical expression for FTIR spectra to estimate OH concentration in several silicate minerals.

$$c_{OH} = \int \frac{K_{(\sigma)}}{150\gamma(3780-\sigma)} d\sigma \quad (2.2)$$

where  $c_{OH}$  is the concentration in mol H/l,  $K_{(\sigma)}$  is the absorption coefficient in cm<sup>-1</sup> at wavenumber  $\sigma$  in cm<sup>-1</sup>, and  $\gamma$  is the anisotropy factor. The integral wavenumber range was from 3000 to 3750 cm<sup>-1</sup>. Because of large anisotropy in olivine

orthorhombic crystal structure,  $\gamma$  for olivine has been used a range between 0.25 to 0.5. Later study used polarized FTIR spectra from *Bell et al.* [2003] suggested largely underestimation of water content in olivine based on Paterson's expression and  $\gamma$  is better between 0.1-0.25. In the present study, it is found that if  $\gamma = 1/3$  in Paterson's equation was used, average OH concentration in wadsleyite from 5 different runs estimated from FTIR spectra revealed excellent agreements with SIMS results (**Fig. 2.3**), suggesting nearly uniform distribution of OH in wadsleyite among three typical orientations.

In the synthesized H-doped wadsleyite crystals, two strong absorption peaks of OH were observed around 3317-3342  $\text{cm}^{-1}$  and 3579-3591  $\text{cm}^{-1}$ , respectively. On the other hand, two strong absorption peaks of OD are located at smaller wavenumbers, around 2465-2477  $\text{cm}^{-1}$  and 2643-2648  $\text{cm}^{-1}$ . This phenomenon could be explained by Hooke's law.

$$\sigma = \frac{1}{2\pi C} \sqrt{\frac{K}{\mu}} \quad \text{and} \quad \mu = \frac{m_1 m_2}{m_1 + m_2} \quad (2.3)$$

where  $\sigma$  is wavenumber,  $C$  is a speed of light,  $K$  is bulk modulus and  $\mu$  is molecular reduced mass. Since  $\mu_{OD}$  is about twice of  $\mu_{OH}$ , ratio of corresponding peak wavenumber between OH and OD is about square root. However, there is a small deviation from  $\sqrt{2}$  about the actual ratio because of difference of elastic coefficient between OH and OD. The absorption peak positions of OH and OD from FTIR spectra of Fe-free wadsleyite yield 1.3539 of a weighted mean value. The useful expression for OD calculation in wadsleyite is showed as below

$$c_{OD} = \int \frac{K(\sigma)}{50(3780/1.3539 - \sigma)} d\sigma \quad (2.4)$$

By integral from 2300 to 2785  $\text{cm}^{-1}$ , calculated OD concentration also showed excellent agreements with SIMS results for 3 runs (**Fig. 2.3**).

### **2.2.3 Determination of Fe concentration by EPMA**

The compositions of Fe-bearing wadsleyite and ringwoodite single crystals were investigated by the electron probe micro-analyzer, EPMA (JEOL JXA8800) in the Institute for Study of the Earth's Interior, Okayama University, under the operating condition of 15 kV and 10 nA specimen current. The standards used for concentration determinations of elements, Mg, Fe and Si, in Fe-bearing wadsleyite and ringwoodite are a natural olivine, locality unknown. Chemical compositions of 3 to 5 synthetic crystals were measured at 6 to 10 points from the center to edge randomly from each crystal. As shown in Table 2, excellent agreement of Mg number among these crystals obtained from the same run confirmed the homogeneity of Fe composition. We detected obvious Fe loss to Pt capsule after slow cooling from 2073 K, and Fe-bearing wadsleyite synthesized in Pt capsules revealed relative high Mg number ( $F_{0.95}$ ). On the other hand, the initial San Carlos olivine composition ( $F_{0.90}$ ) was well preserved in crystals of Fe-bearing wadsleyite and ringwoodite recovered from Au capsules.

## **2.3 H-D exchange experiments**

### **2.3.1 Determination of typical orientations of wadsleyite single crystals**

Unlike the ringwoodite having an 'isometric hexoctahedral' spinel structure, wadsleyite has orthorhombic crystal structure with lattice parameter  $a=5.71\text{\AA}$ ,  $b=11.47\text{\AA}$ ,  $c=8.27\text{\AA}$ . Modified-spinel structure in wadsleyite can generate anisotropy

of hydrogen diffusion along three principle orientations. To determine anisotropy of hydrogen diffusion in wadsleyite, determination of crystallographic orientations was necessary before H-D inter-diffusion experiments.

The orientation of wadsleyite single crystals was determined by a precession camera installed at the Institute for Study of the Earth's Interior, Okayama University. Characteristic spectrum is Mo\_K $\alpha$  with wavelength  $\lambda=0.7107$  Å and exposure time is 6 min. When the negative plate exercises conical motion from  $-20^\circ$  to  $20^\circ$ , X-ray emits through single crystal with continuous variation of incident orientation and thus products representative diffraction patterns in the negative plate. By adjust single crystals from three dimensions, we could obtain typical diffraction patterns for three principle orientations of wadsleyite. Regular operated voltage and current are 30 kV and 24 mA, respectively. If the single crystals are small, we will increase operated condition to 40 kV and 30 mA to obtain legible diffraction patterns. **Fig. 2.4** exhibits X-ray diffraction patterns of three principle orientations of wadsleyite single crystals.

### **2.3.2 H-D inter-diffusion experiments**

For H-D inter-diffusion in Fe-free wadslyite, two groups of H- and D-doped pairs were used: (1) 5k2141 - 1k1710 and (2) 5k2033 - 5k2038. Most inter-diffusion experiments in Fe-free wadsleyite were conducted using crystals from the first pair. For the second diffusion couple, single crystals grown from KMC solvent have lower water content, while the difference of total water content between H- and D-doped crystals is smaller than the first pair (**Table 2.2**). Several high-quality inclusion-free pairs from 5k2033 and 5k2038 were chosen to investigate water dependence on H-D

inter-diffusion.

For the H-D inter-diffusion in Fe-bearing wadsleyite, two groups of H- and D-doped pairs were also used: (1) 5k2300 and 1k1890 (2) 5k2227 and 5k2230. FTIR analysis of the synthesized crystal showed similar total water contents in each wadsleyite crystal pair, while EPMA analysis revealed higher Fe content in the first pair (**Table 2.2**). Most inter-diffusion experiments in Fe-bearing wadsleyite were conducted using crystals from the first diffusion couple and one additional experiment with crystal pair from the second group was conducted to investigate the Fe dependence on hydrogen self-diffusivities.

For H-D inter-diffusion of Fe-bearing ringwoodite, single crystal pairs from 5k2367 and 5k2370 were used. The bulk water content in D-doped ringwoodite is 30% lower than that of H-doped one, although their synthesis conditions are completely same (**Table 2.2**).

A pair of H- and D-doped wadsleyite or ringwoodite crystals was put together into gold capsule (inner diameter is 1.8 mm and length is 2 mm) and fine-grained gold powder (1  $\mu\text{m}$ ) was used to fill up the remaining space (**Fig. 2.5**). After determination of crystallographic orientation, each crystal was double-polished with 1- $\mu\text{m}$  diamond paste and tightly coupled together. The one end of Au capsule was welded and the opposite end was covered by a gold foil. Cr-doped MgO octahedron with edge length of 14 and 10 mm and tungsten carbide cubes with 6 and 5 mm of truncation edge length were used for diffusion experiments in wadsleyite and ringwoodite, respectively. Because of short length of crystal pair ( $< 0.7$  mm), temperature gradient

seems to be not crucial, although straight  $\text{LaCrO}_3$  heaters were used for diffusion experiments. The Au capsule was kept at 353 K in a vacuum oven for  $\sim 8$  hours, and then the Au capsule surrounded by MgO was loaded in a  $\text{LaCrO}_3$  cylindrical heater with 1.3 mm thickness. The center of the capsule along the cylindrical direction was shifted to  $\sim 0.75$  mm from the center of the heater along the axial direction to realize the temperature indicated by the  $\text{W}_{97}\text{Re}_3$ - $\text{W}_{75}\text{Re}_{25}$  thermocouple, which had the same distance from center of the heater (**Fig. 2.5**).

The diffusion experiments were conducted at the same pressure as synthesis in either 1000 or 5000 ton Kawai-type Multi-anvil apparatus and at variable temperatures from 1000 to 1400 K. To minimize diffusion during heating up to the target temperature, the controlled-heating rate was setting up to higher than 10 K/s. After annealing at the target temperatures, the samples were quenched to room temperature. Then the press load was released slowly. The recovered samples were polished to the center of crystal pairs and then mounted in Bi-Sn alloy to minimize the hydrogen contamination from background during SIMS analysis.

### **2.3.3 SIMS measurements**

Recovered capsules were polished to the center of crystal couples and then mounted in Bi-Sn alloy to minimize the hydrogen contamination from background during following SIMS profile determinations. D-H inter-diffusion profiles across a diffusion couple were determined by SIMS, Cameca 6F and 1270 at Hokkaido University. The mounts were coated with Au layer of  $\sim 30$  nm by plasma sputtering. Diffusion profiles were obtained along an array of spot analyses from one crystal edge

to another crystal edge perpendicular to the interface (**Fig. 3.1**). The polished surfaces were coated with Au layer of ~30 nm by plasma sputtering. A primary Cs<sup>+</sup> ion beam operated at 17-20 nA, and was focused to form a 20~30 μm spot on the sample, and the secondary <sup>1</sup>H<sup>-</sup>, <sup>2</sup>H<sup>-</sup> and <sup>30</sup>Si<sup>-</sup> ions were collected from the center region (10 μm in diameter) of the sputtered area using a mechanical aperture to minimize artifacts arising from hydrogen adsorption on the polished sample surface. A normal incident electron flood gun was used for charge compensation. The entrance and exit slits were narrowed enough to minimize the contribution of <sup>28</sup>Si<sup>2</sup>H<sup>-</sup> to the <sup>30</sup>Si<sup>-</sup>. Standard for line analysis was not used because absolute concentrations are not required to determine diffusion coefficients. Although *Du Frane and Tyburczy* [2012] could not obtain the qualitative <sup>1</sup>H profile because of low water solubility in olivine at 2 GPa, amplifying influence from background, the present measurement setting can allow obtaining the <sup>1</sup>H line profile with counts higher than the background.

**Table 2.1.** Synthesis runs conducted in a Kawai-type multi-anvil apparatus

Run.		P(GPa)	solvent	silcate	capsule	largest grain size (mm)
5k2038	H-wad	16	KMC+5wt.%H2O	Fo	Pt	1.0
5k2033	D-wad	16	KMC+5wt.%H2O	Fo	Pt	0.9
5k2141	H-wad	16	Fo+6wt.%H2O	Fo90	Pt	1.2
1k1710	D-wad	16	Fo+6wt.%H2O	Fo90	Pt	1.2
5k2227	H-Fe-wad	16	Fo85+6wt.%H2O	Fo90	Pt	1.8
5k2230	D-Fe-wad	16	Fo85+6wt.%H2O	Fo90	Pt	1.8
1K1890	H-Fe-wad	16	Fo85+6wt.%H2O	Fo90	Au	1.5
5K2300	D-Fe-wad	16	Fo85+6wt.%H2O	Fo90	Au	1.8
5K2367	H-Fe-rw	20	Fo85+6wt.%H2O	Fo90	Au	1.4
5K2370	D-Fe-rw	20	Fo85+6wt.%H2O	Fo90	Au	1.8

**Table 2.2.** Fe and water content in H-doped and D-doped wadsleyite and ringwoodite single crystals determined by EPMA, FTIR and SIMS.

Run.		Mg#	FTIR		SIMS	
			D/(H+D)	Total/wt%	D/(H+D)	Total/wt.%
5k2038	H-wad	100.00	n.d.	0.51±0.02	n.d.	0.51±0.00
5k2033	D-wad	100.00	0.52±0.01	0.60±0.02	0.49±0.00	0.61±0.00
5k2141	H-wad	100.00	n.d.	0.97±0.05	n.d.	1.05±0.08
1k1710	D-wad	100.00	0.77±0.01	0.58±0.03	0.76±0.02	0.56±0.03
5k2227	H-Fe-wad		n.d.	1.26±0.04		
5k2230	D-Fe-wad		0.80±0.00	0.95±0.01	0.81±0.01	1.01±0.00
1K1890	H-Fe-wad	90.27±0.39	n.d.	0.95±0.03		
5K2300	D-Fe-wad	90.02±0.19	0.78±0.01	1.04±0.02		
5K2367	H-Fe-rw	90.43±0.11			n.d.	0.77±0.04
5K2370	D-Fe-rw	90.95±0.18			0.78±0.00	0.55±0.05

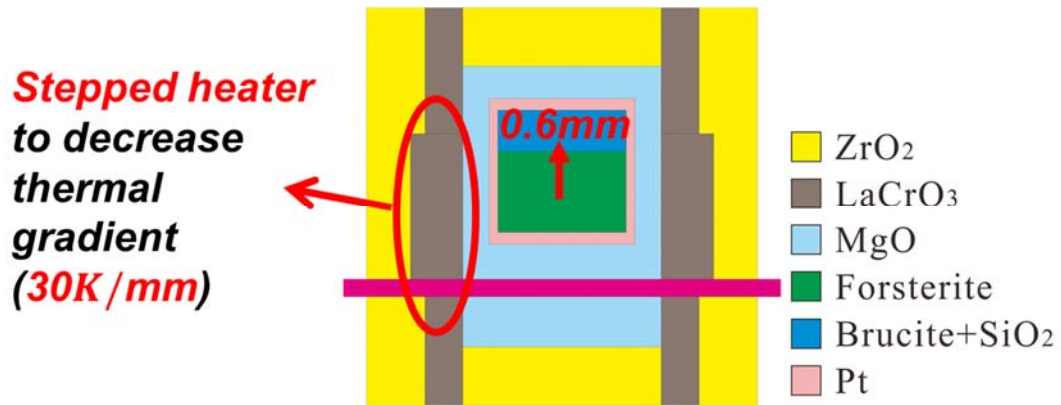


**Fig. 2.1.** 14/6 assembly for synthesis of Fe-free wadsleyite.

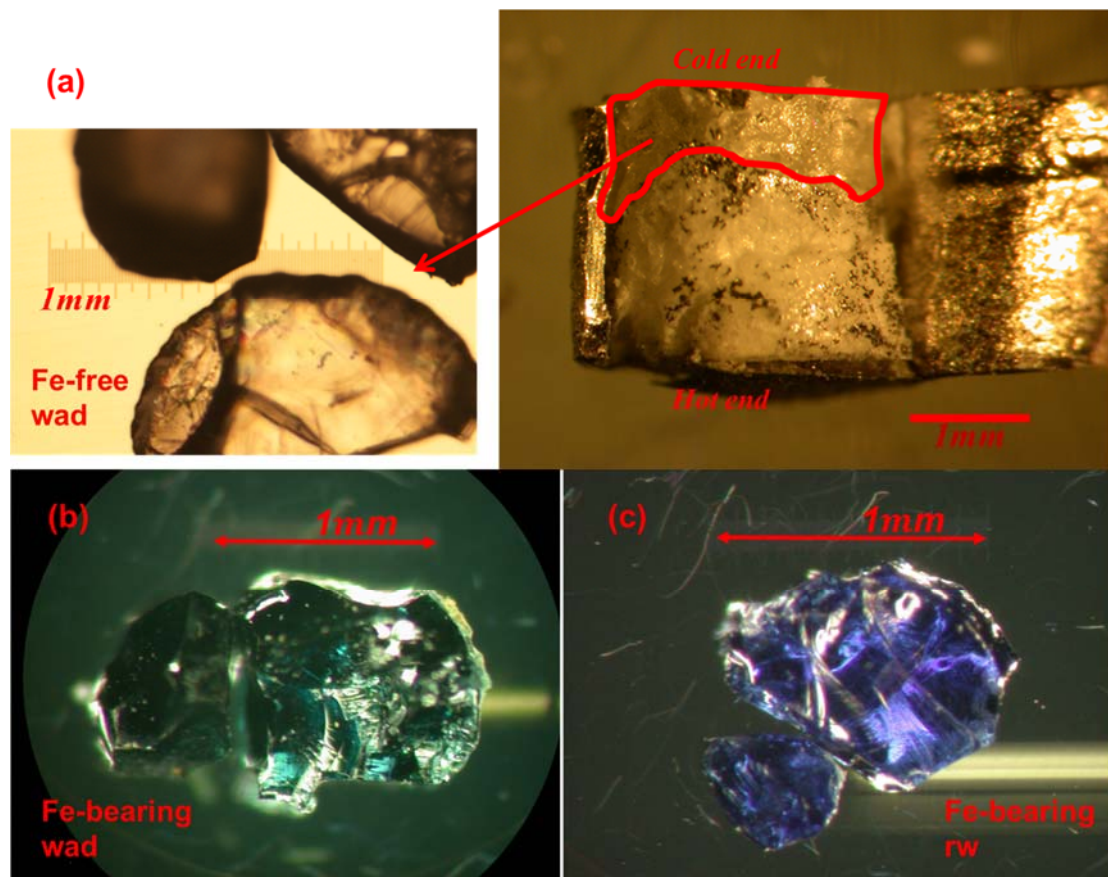


**Fig. 2.2.** Examples of large single crystals of (a) Fe-free wadsleyite, (b) Fe-bearing wadsleyite and (c) Fe-bearing ringwoodite.

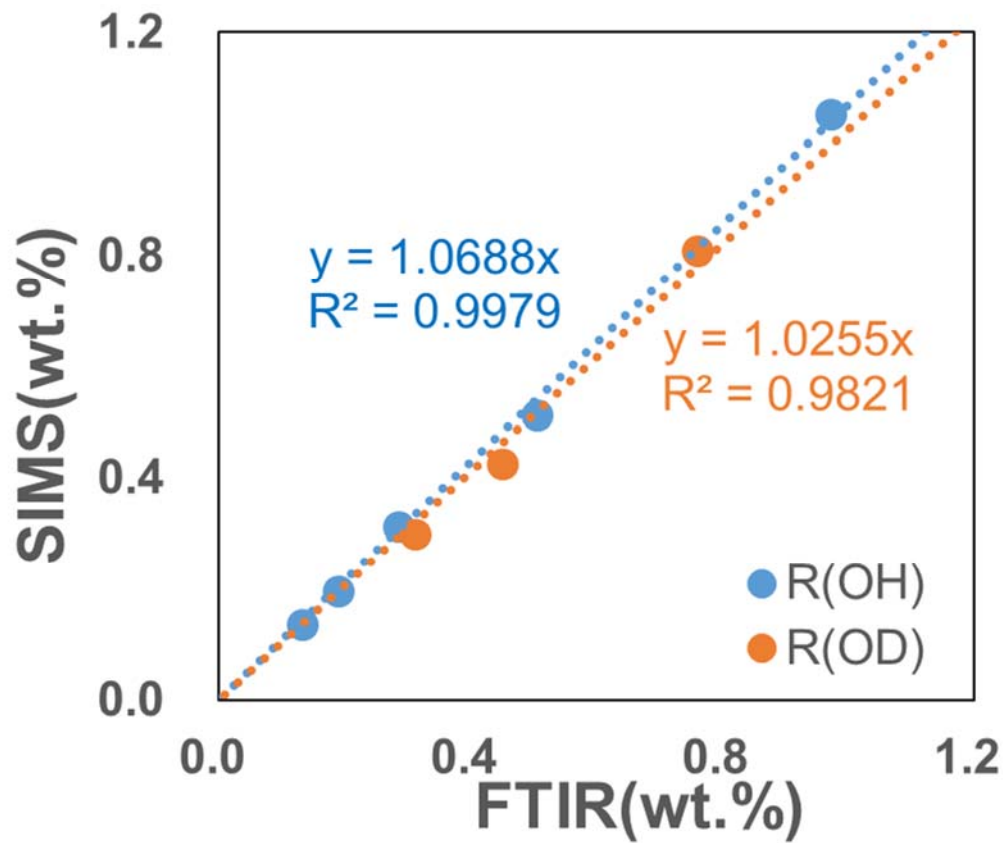


**Fig. 2.3.** Comparisons of OH concentrations in wadsleyite (blue points) and OD concentrations (orange points) between FTIR and SIMS determinations, respectively.

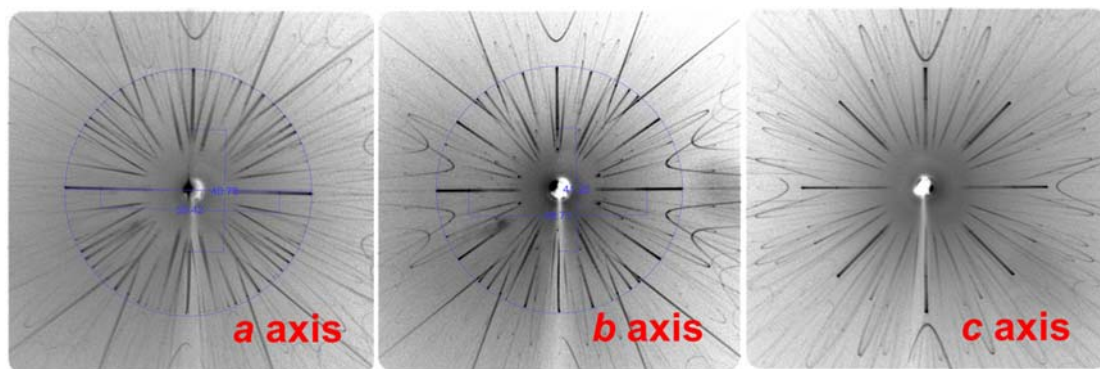


**Fig. 2.4.** Typical XRD image of wadsleyite of three orientations.

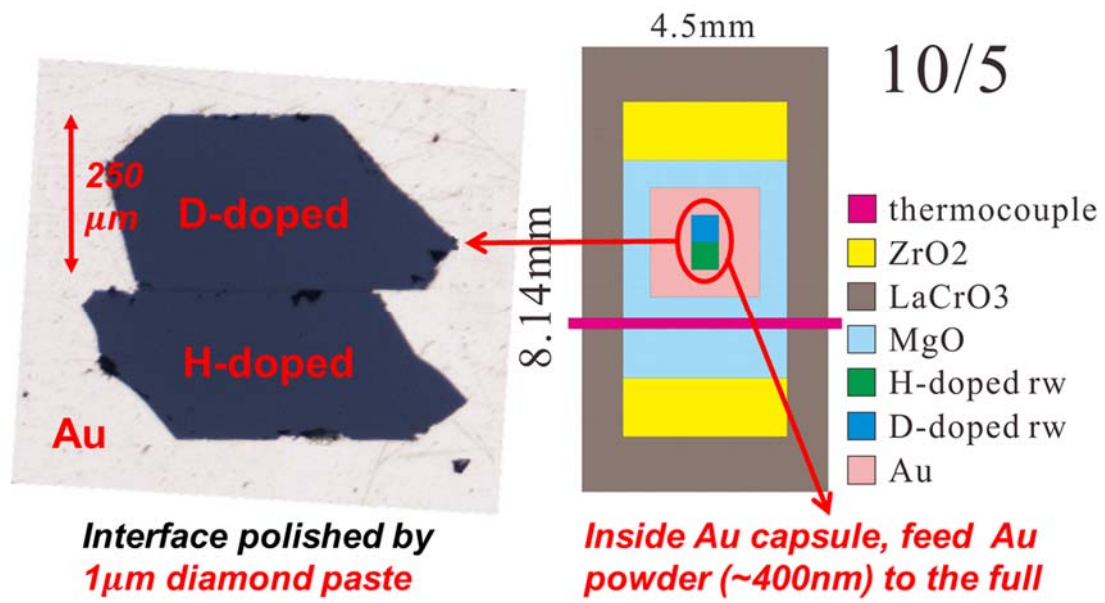


Fig. 2.5. 10/5 assembly for H-D inter-diffusion in Fe-bearing ringwoodite.

## Chapter 3

### Results of H-D inter-diffusion in wadsleyite and ringwoodite

#### 3.1 H-D inter-diffusion in Fe-bearing ringwoodite

Fig. 3.1 shows a representative diffusion profile in Fe-bearing ringwoodite from Run. 5K2587. The diffusion profile of total concentration (H + D) is much shorter than H-D inter-diffusion profile, suggesting that the influence of concentration diffusion is negligible compared to the H-D inter-diffusion. Gold is an excellent material to protect destruction of crystals during compression and has an ability to prevent water loss at high temperature but it cannot hinder the H-D exchange at the crystal edges. As shown in Fig. 4.2, the diffusion profile in the D-doped crystal revealed a symmetrical profile at both sides of the crystal edge. A diffusion profile in the D-doped crystal at the opposite side of the interface between D and H-doped crystals was not observed in the H-doped crystal. Although the diffusion couples were pre-baked at 353K for more than 8 hours in a vacuum oven just before compression, there was still small amount of water residing in gold powder. At high temperatures, this residual water with natural isotopic composition exchanged with the D-doped crystal at the edge.

All D/(D+H) profiles were analyzed using 1-D solutions to Fick's second law for a semi-infinite material [*Carslaw and Jaeger*, 1959; *Crank*, 1975]. Since H-D inter-diffusion diffusion profile across the interface is symmetrical in shape, H-D inter-diffusion coefficient is assumed to be approximately equal to hydrogen

self-diffusivity. Concentration along  $x$  direction perpendicular to the interface is

$$\frac{C(x,t)-C_0}{C_1-C_0} = \frac{1}{2} \operatorname{erfc}\left(\frac{x}{2\sqrt{D_H t}}\right) \quad (3.1)$$

where  $C(x,t)$  is the normalized fraction at distance  $x$  (m) and time  $t$  (s),  $C_0$  is the initial concentration (set to 0), and  $C_1$  is the concentration at the crystal center where the concentration is the maximum (i.e., set to 1),  $D_H$  is hydrogen self-diffusion coefficient.

The logarithmic diffusion coefficient linearly decreases as a function of the reciprocal temperature, which can be fitted by the Arrhenian formula:

$$\log D_{H(T)} = \log D_0 - \frac{H_a}{2.303*RT} \quad (3.2)$$

where  $D_0$  is the pre-exponential factor ( $\text{m}^2/\text{s}$ ),  $H_a$  is the activation enthalpy ( $\text{kJ/mol}$ ),  $R$  is the Gas constant ( $\text{J/K}$ ) and  $T$  is the absolute temperature ( $\text{K}$ ). By fitting of all data of hydrogen self-diffusion coefficients to the Arrhenius equation, the parameters were determined to be the pre-exponential term,  $D_0 = 10^{-7.29 \pm 0.46} \text{ m}^2/\text{s}$  and activation enthalpy,  $H_a = 101 \pm 10 \text{ kJ/mol}$  at 21 GPa in hydrous ringwoodite (**Fig. 3.2**). The diffusion profiles reveal symmetrical characteristic although the total water contents in H-doped crystals are 40% higher than those in D-doped ones, suggesting an insignificant influence of water concentration on the hydrogen self-diffusivity.

## 3.2 H-D inter-diffusion in Fe-bearing wadsleyite

### 3.2.1 H-D inter-diffusion in wadsleyite with high Fe content (Mg#90)

**Fig. 3.3** shows a representative diffusion profile in Fe-bearing wadsleyite (Mg#90) from Run. 5K2493. Total H+D concentration profile in wadsleyite diffusion couple is

nearly flat from one crystal to another, which are consistent with results of FTIR measurements for the synthesized crystals. 1-D solutions to Fick's second law for a semi-infinite crystal is also suitable to simulate symmetrical profiles in Fe-bearing wadsleyite. The hydrogen self-diffusion coefficients are plotted as a function of reciprocal temperature in **Fig. 3.4**. The hydrogen self-diffusion coefficients increase with increasing temperature for each crystallographic direction. The absolute values are different for each crystallographic orientation, and yields the highest mobility of hydrogen self-diffusion along *a*-axis and the lowest along *c*-axis in the experimental temperature range. The linear relation in Arrhenian plot indicates that diffusion in wadsleyite is controlled by thermally activated process, and allows us to determine the parameters  $D_0$  and  $H$  as follows,

$$D_{H(001)} = 10^{-8.26 \pm 0.33} * \exp\left(-\frac{75 \pm 6 \text{ kJ/mol}}{2.303 * RT}\right) \text{ m}^2/\text{s} \quad (3.3)$$

$$D_{H(010)} = 10^{-5.74 \pm 0.48} * \exp\left(-\frac{142 \pm 10 \text{ kJ/mol}}{2.303 * RT}\right) \text{ m}^2/\text{s} \quad (3.4)$$

$$D_{H(100)} = 10^{-7.44 \pm 0.90} * \exp\left(-\frac{100 \pm 19 \text{ kJ/mol}}{2.303 * RT}\right) \text{ m}^2/\text{s}. \quad (3.5)$$

The  $H$  increases from 75 to 142 kJ/mol in an order of (001), (100) and (010), while the  $D_0$  increases in the opposite order. Since the highest activation enthalpy for hydrogen diffusion was obtained along the slowest crystallographic orientation, there is only small anisotropy of hydrogen self-diffusion at temperatures relevant to the mantle transition zone.

Geometric average of three principle crystal orientations yields the pre-exponential term,  $D_0 = 10^{-7.15 \pm 0.46} \text{ m}^2/\text{s}$ , and the activation enthalpy,  $H_a = 106 \pm 11 \text{ kJ/mol}$ , at 16 GPa (**Fig. 3.2**). The hydrogen diffusivity in Fe-bearing

wadsleyite at 16 GPa is negligibly small with Fe-bearing ringwoodite at 21 GPa and about 1 order of magnitude higher than that of olivine determined at 2 GPa from *Du Frane and Tyburczy* [2012] (**Fig. 3.2**). On the other hand, hydrogen diffusion coefficients in wadsleyite and ringwoodite are several orders of magnitude higher than diffusion coefficients of Si and O from *Shimojuku et al.* [2009] at the same temperatures.

### **3.2.2 H-D inter-diffusion in wadsleyite with low Fe content (Mg#95)**

**Fig. 3.5** shows the H-D inter-diffusion profile in Fe-bearing wadsleyite (Mg#95) normalized to  $a$ -axis at 1200 K and 16 GPa (Run. 5K2802). Total (H+D) concentration in H-doped wadsleyite is a little higher than D-doped one, which is consistent with results of FTIR measurements obtained from the synthesized crystals. The diffusion profile reveals similar but asymmetric than Fe-free wadsleyite. The 1-D solution of Fick's second law was also used to simulate diffusion profiles in Fe-bearing wadsleyite (Mg#95). Fitting result yields  $\sim 0.7$  order of magnitude lower than diffusivity from wadsleyite with higher Fe content at the same condition (**Fig. 3.6**).

### **3.3 H-D inter-diffusion in Fe-free wadsleyite**

**Fig. 3.7** shows a representative H-D diffusion profile in Fe-free wadsleyite from Run. 1K2409. Total H and D concentration diffusion profiles are much shorter than H-D inter-diffusion profiles, suggesting that the influence of concentration diffusion is negligible compared to the H-D inter-diffusion though bulk water content in D-doped

crystals is ~40% lower than H-doped ones for 5k2141 and 1k1710 pairs. H-D exchange profiles between crystals and water with natural isotopic composition residing in gold powder were also found at the crystal edges (the opposite side of the interface between two wadsleyite crystals, **Fig. 3.7**).

All D/(D+H) profiles in Fe-free wadsleyite revealed obviously asymmetric shape (**Fig. 3.8**). Diffusion length in the H-doped crystals seems to be longer than length in the D-doped ones, suggesting that deuterium self-diffusion in Fe-free wadsleyite is distinctly faster than hydrogen self-diffusion. Thus, analyzed method using Fe-bearing symmetric profiles is not suitable to apply the diffusion profile analysis for the Fe-free asymmetric ones. We introduced Finite-difference numerical simulation similar to the method available in former Fe-Mg inter-diffusion asymmetric profile studies (ref.) based on an empirical expression:

$$D_{(x,t)} = D_0 \cdot \exp\left(a \cdot C_{(x,t)} \cdot \frac{\partial C_{(x,t)}}{\partial x}\right) \quad (3.6)$$

where  $D_{(x)}$  is deuterium profile diffusion coefficient at profile position  $x$  and time  $t$ ,  $D_0$  is deuterium self-diffusion coefficient in Fe-free wadslyite,  $C_{(x,t)}$  is normalized deuterium concentration at profile position  $x$  and time  $t$  and  $a$  is asymmetric factor indicate the differences between hydrogen and deuterium diffusivities. Profile smooth function is introduced from former asymmetric studies [*Petry, 1999, Mackwell et al., 2004*]:

$$C_{(x)} = \frac{P_1}{(1 + \exp(P_2 - P_3 x))^{1/P_4}} \quad (3.7)$$

where  $P_1$ ,  $P_2$ ,  $P_3$  and  $P_4$  is smoothing constant. The step-by-step algorithm (**Eq. 3.8**) were conducted by Fortran language with five self-consistent loops:  $x$ ,  $C_{(x,t)}$ ,  $a$ ,

$D_0$ ,  $I$ , where  $I$  indicates interface migration length.

$$\frac{\partial C}{\partial t} = a \cdot D_0 \cdot \exp(a \cdot C_{(x)}) \left(\frac{\partial C}{\partial x}\right)^2 + D_0 \cdot \exp(a \cdot C_{(x)}) \frac{\partial^2 C}{\partial x^2} \quad (3.8)$$

with error function is

$$\sum \frac{(C_{f(x)} - C_{r(x)})^2}{n} \quad (3.9)$$

where  $C_{f(x)}$  and  $C_{r(x)}$  is simulation deuterium concentration at profile position  $x$  after experimental duration and experimental deuterium concentration, respectively,  $n$  is simulation nodes number.

Numerical simulation results showed similar asymmetric factors at various temperatures and for three principle orientations,  $a = -2.64 \pm 0.29$ . A presence of the single consistent value suggests that deuterium self-diffusion in Fe-free wadsleyite is about one order faster than hydrogen. The diffusion for both isotopes showed a linear relationship against the reciprocal temperature (**Fig. 3.9**). The determined hydrogen and deuterium diffusion coefficients were fitted to the Arrhenius equation. The pre-exponential term  $D_0$  and activation enthalpy  $H_a$  at 16 GPa in Fe-bearing wadsleyite were calculated as follows:

$$D_{H(100)} = 10^{-6.15} * \exp\left(-\frac{166 \text{ kJ/mol}}{2.303*RT}\right) \text{ m}^2/\text{s} \quad (3.10)$$

$$D_{H(010)} = 10^{-7.57} * \exp\left(-\frac{154 \text{ kJ/mol}}{2.303*RT}\right) \text{ m}^2/\text{s} \quad (3.11)$$

$$D_{H(001)} = 10^{-6.83} * \exp\left(-\frac{155 \text{ kJ/mol}}{2.303*RT}\right) \text{ m}^2/\text{s} \quad (3.12)$$

$$D_{D(100)} = 10^{-5.59} * \exp\left(-\frac{152 \text{ kJ/mol}}{2.303*RT}\right) \text{ m}^2/\text{s} \quad (3.13)$$

$$D_{D(010)} = 10^{-6.27} * \exp\left(-\frac{157 \text{ kJ/mol}}{2.303*RT}\right) \text{ m}^2/\text{s} \quad (3.14)$$

$$D_{D(001)} = 10^{-5.78} * \exp\left(-\frac{155 \text{ kJ/mol}}{2.303*RT}\right) \text{ m}^2/\text{s} \quad (3.15)$$

The variation of  $H_a$  for each isotope is quite small and in a range between 150 and

170 kJ/mol. In addition,  $H_a$  for each principle crystallographic directions are almost constant. In contrast,  $D_0$  for H are nearly one order of magnitude smaller than that for D.

Geometric average of three principle crystal orientations in Fe-free wadsleyite yields the pre-exponential term,  $D_0 = 10^{-6.85}$  and  $10^{-5.88}$  m<sup>2</sup>/s, and the activation enthalpy,  $H_a = 158$  and  $155$  kJ/mol for hydrogen and deuterium diffusion in Fe-free wadslyite at 16 GPa, respectively. Hydrogen diffusion in Fe-free wadsleyite has the same anisotropy and ~1 order of magnitude lower than deuterium diffusion.

This study demonstrates that influence of difference of water content between H- and D-doped pairs on the diffusivity is negligibly small because diffusion profiles of bulk water diffusion are much shorter than those of H-D inter-diffusion profiles. Asymmetric feature of diffusion profile from Fe-free wadsleyite is not attributed to water content dependence since parallel experiments conducted in 5k2033 and 5k2038 pairs, which have similar water content in H- and D-doped crystals (**Table 2.2**), also produced obvious asymmetric profiles and similar simulation asymmetric factor (**Fig. 3.10**). On the other hand, H-D inter-diffusion experiments in Fe-bearing ringwoodite behave 30% higher water content in H-doped ringwoodite than D-doped ones (**Table 2.2**), similar to 5k2141 and 1k1710 Fe-free wadsleyite pairs, but inter-diffusion profiles are symmetric (**Fig. 3.1**). These comparisons suggest observed asymmetric inter-diffusion profiles in Fe-free wadsleyite might depend on variations of chemistry point defects adjusting to the Fe concentration instead of difference of water content in crystal pairs.

**Table 3.1.** H-D inter-diffusion runs conducted in a Kawai-type multi-anvil apparatus

<b>Fe-bearing ringwoodite</b>							
<b>Run.</b>	<b>axis</b>	<b>Mg#</b>	<b>T(K)</b>	<b>P(GPa)</b>	<b>dur(min)</b>	<b>logD<sub>H</sub>(m<sup>2</sup>/s)</b>	<b>a</b>
5k2515		91	1000	21	51	-12.51	0
5k2534		91	1000	21	30	-12.60	0
5k2535		91	1100	21	17	-12.21	0
5k2586		91	1200	21	8	-11.58	0
5k2587		91	1300	21	4	-11.39	0
<b>Fe-bearing wadsleyite</b>							
1k1943	<i>a</i>	90	1200	16	21	-11.55	0
1k2066	<i>b</i>	90	1000	16	124	-13.07	0
1k2075	<i>b</i>	90	1100	16	41	-12.51	0
1k2102	<i>c</i>	90	1000	16	132	-12.60	0
5k2493	<i>b</i>	90	1000	16	90	-13.20	0
1k2181	<i>b</i>	90	1200	16	5	-11.89	0
1k2184	<i>a</i>	90	1100	16	12	-11.83	0
1k2193	<i>c</i>	90	1200	16	5	-11.73	0
1k2198	<i>c</i>	90	1100	16	11	-12.27	0
1k2403	<i>a</i>	90	1000	16	77	-12.20	0
5k2802	<i>a</i>	95	1200	16	12	-12.40	<0
<b>Fe-free wadsleyite</b>							
1k1717	<i>b</i>	100	1200	16	12	-13.92	-2.7
1k1782	<i>c</i>	100	1200	16	13	-13.57	-2.0
1k1789	<i>b</i>	100	1200	16	13	-14.27	-2.7
1k1790	<i>a</i>	100	1300	16	8	-13.00	-2.6
1k1791	<i>c</i>	100	1000	16	104	-14.92	-2.8
1k1872	<i>a</i>	100	1200	16	22	-13.15	-2.6
5k2266	<i>a</i>	100	1000	16	280	-14.89	-3.0
1k2049	<i>b</i>	100	1000	16	1020	-15.61	-2.6

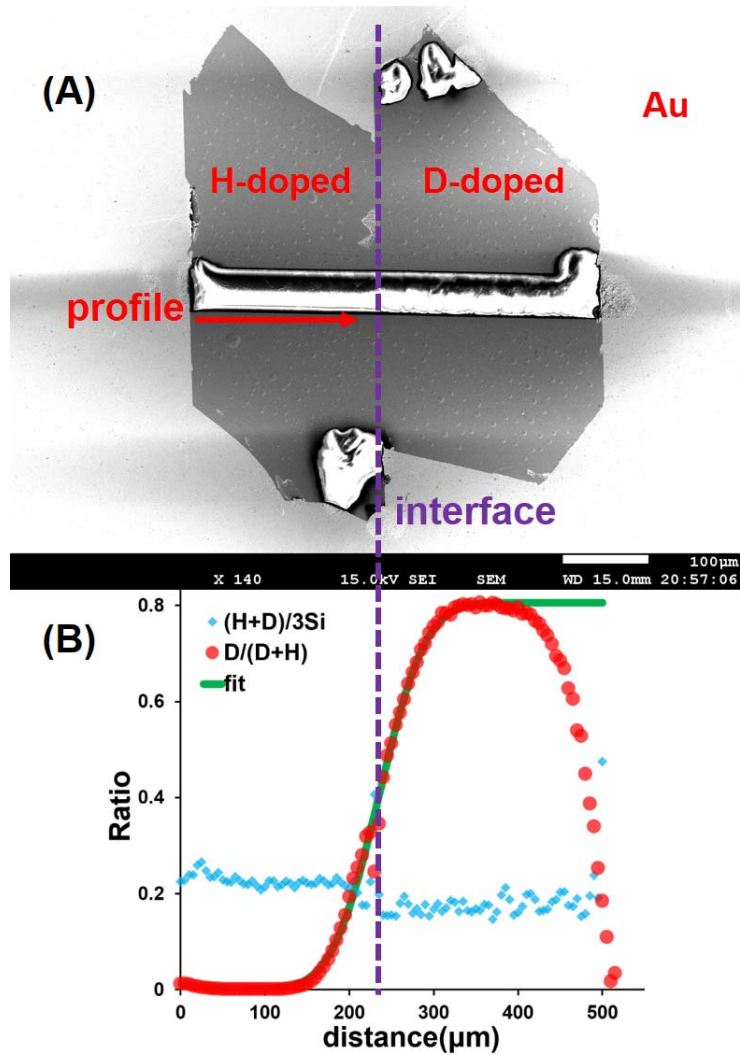


**Fig. 3.1.** An example of diffusion profile in Fe-bearing ringwoodite from 5K2587 measured by SIMS. **(A)** SEM micrograph of sample showing array of craters from SIMS spot line analyses. **(B)** Diffusion profiles from one crystal edge to another crystal edge perpendicular to the interface on the polished surface. Red squares denote a line profile of  $D/(D+H)$  for calculating the diffusion coefficients. In the edge of the D-doped crystal, unavoidable exchange with  $H_2O$  in surrounding Au generated another diffusion profile similar to the interface one. However,  $D/(D+H)$  almost remains constant concentration, which is same as that of the sample before the H/D diffusion experiments. Therefore, a part of constant concentration was defined to be initial concentration for fitting. Blue diamond indicates a line profile of  $(H+D)/3Si$  ratios calculated from sum total counts of H and D divided by three times of  $^{29}Si$  counts, which represent the variation of total water content in the profile.

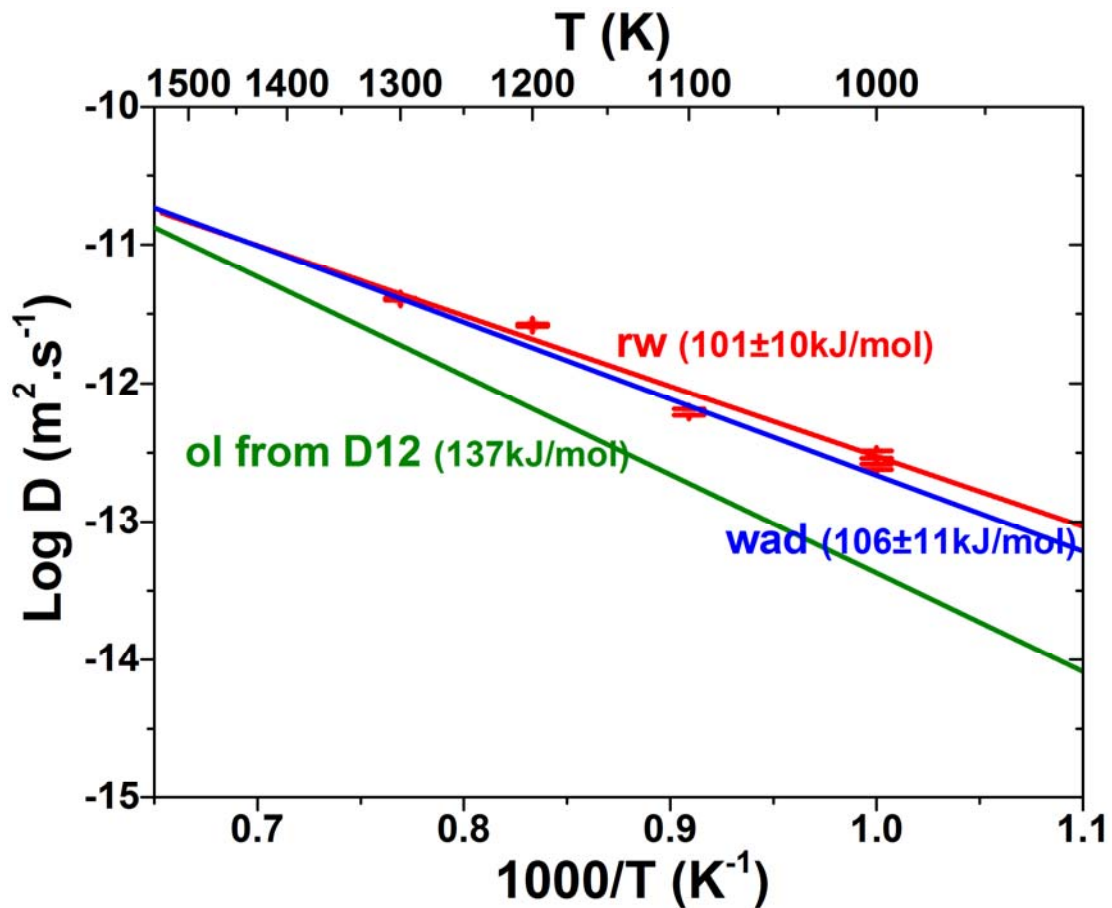


**Fig. 3.2.** Arrhenius plot of hydrogen self-diffusion in Fe-bearing ringwoodite and comparison with hydrogen self-diffusion in Fe-bearing wadsleyite, and olivine from previous study. The red symbols represent the diffusion coefficients obtained at different temperatures calculated from 1-D solutions to Fick's second law, respectively. The red line is a linear regression of the data at 21 GPa. The fit of Eq. (3.2) to the experimental data for hydrogen self-diffusivity of Fe-bearing ringwoodite at 21 GPa yields activation energy  $H_a = 101 \pm 10$  kJ/mol and  $D_0 = 10^{-7.29 \pm 0.46}$  m<sup>2</sup>/s. Dark blue line shows the geometric mean of hydrogen self-diffusivities of three orientations in Fe-bearing wadsleyite of this study at 16 GPa with  $H_a = 106 \pm 11$  kJ/mol and  $D_0 = 10^{-7.15 \pm 0.46}$  m<sup>2</sup>/s. Green line displays the geometric mean of hydrogen self-diffusivities in olivine at 2 GPa [Du Frane and Tyburczy, 2012].

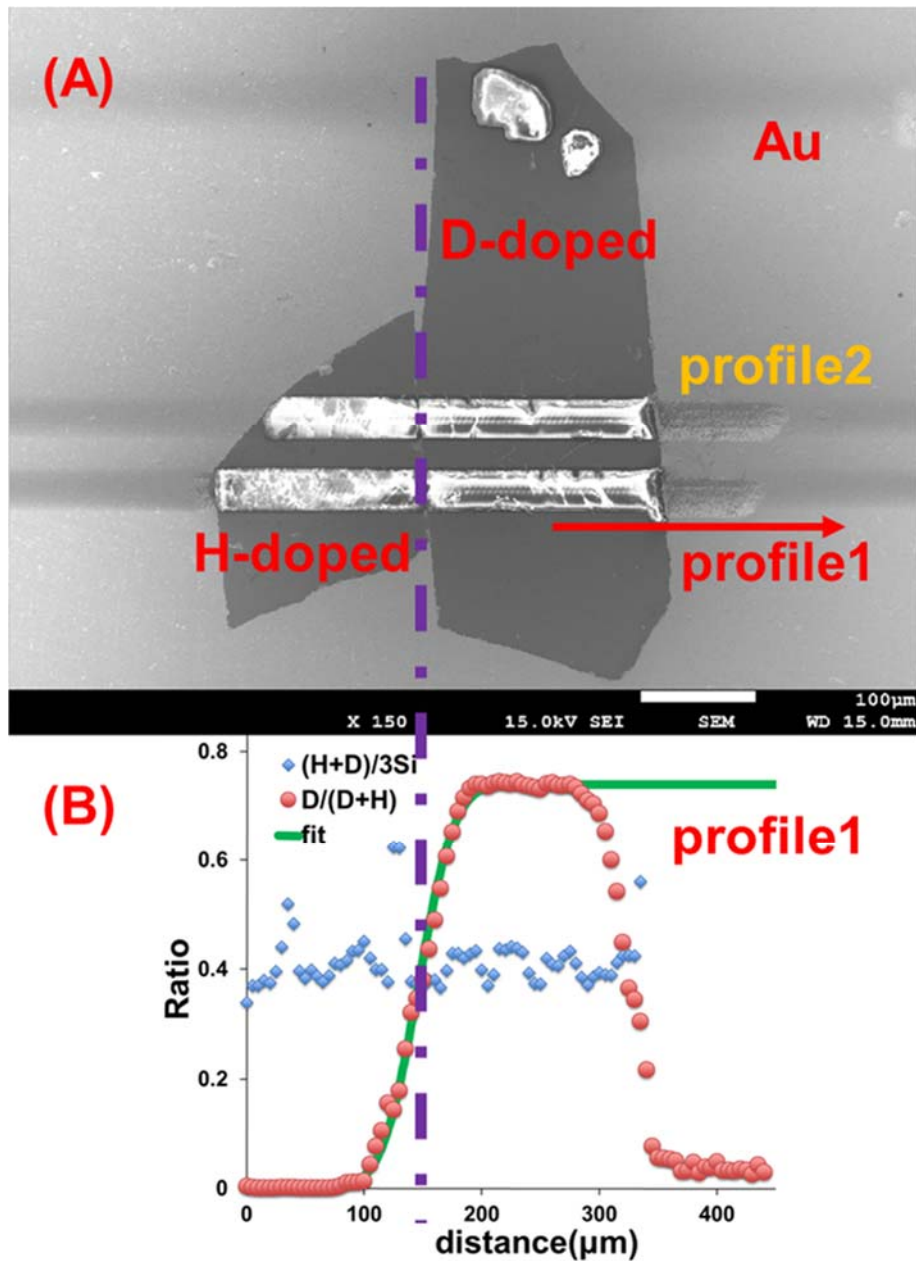


**Fig. 3.3.** An example of diffusion profile in Fe-bearing wadsleyite (Mg#90) from Run. 5K2493 measured by SIMS. (A) SEM micrograph of sample (5K2493) showing array of craters from SIMS spot line analyses. (B) Diffusion profile 1 from one crystal edge to another crystal edge perpendicular to the interface on the polished surface.

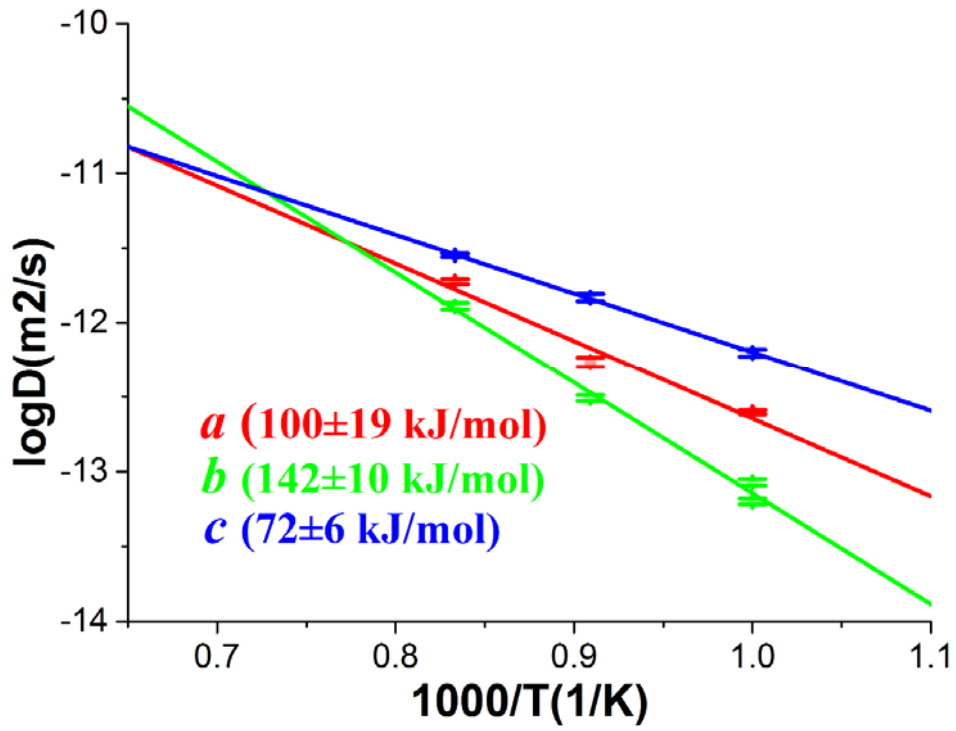


**Fig. 3.4.** Arrhenius plot of hydrogen self-diffusion in Fe-bearing for three principle crystallographic orientations.

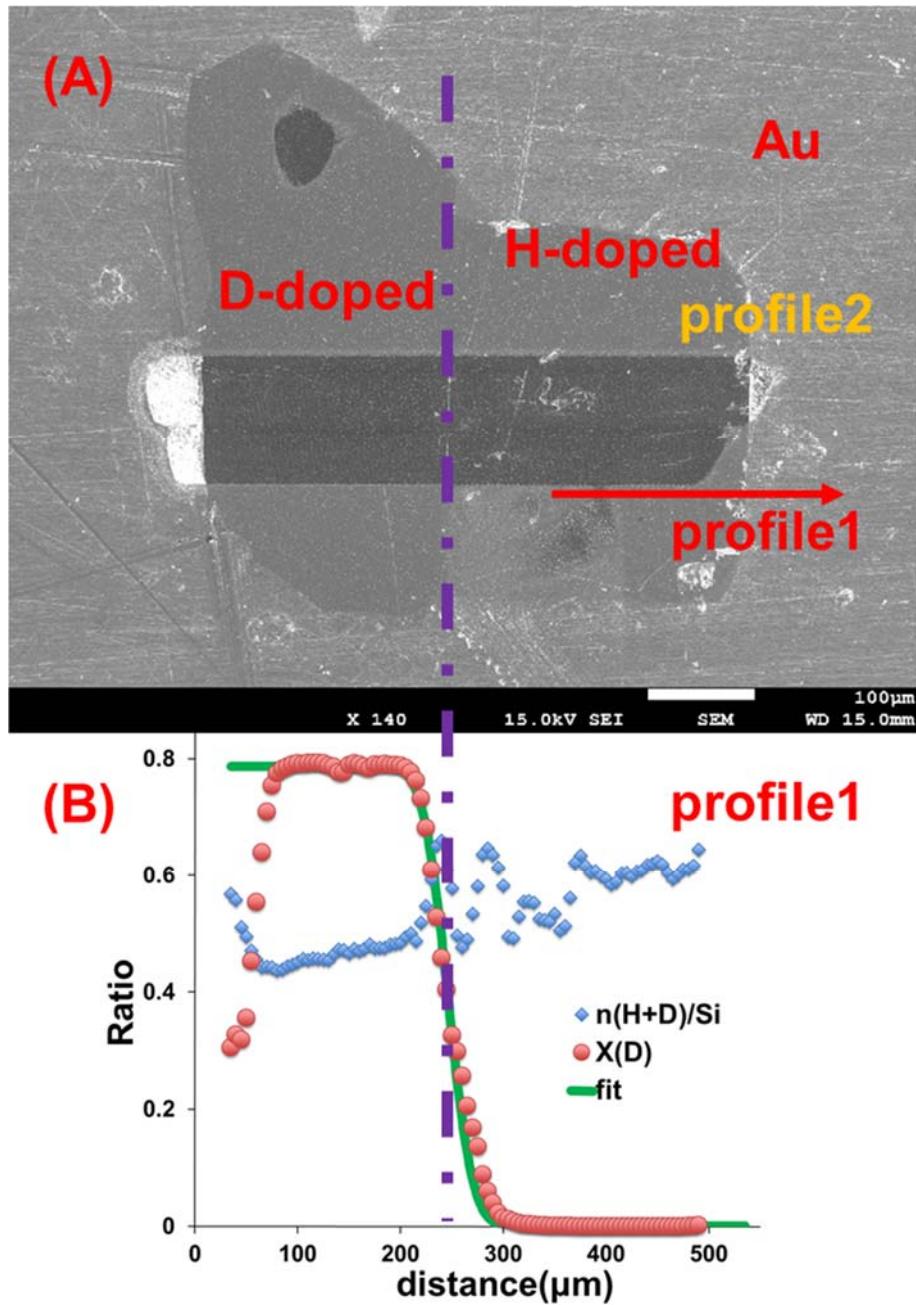


**Fig. 3.5.** Inter-diffusion profile in Fe-bearing wadsleyite (Mg#95) normalized to  $a$ -axis at 1200K, 16 GPa from Run. 5K2802 measured by SIMS. **(A)** SEM micrograph of sample showing array of craters from SIMS spot line analyses. **(B)** Diffusion profile 1 from one crystal edge to another crystal edge perpendicular to the interface on the polished surface. The diffusion profile reveals similar but obviously smaller asymmetric property than Fe-free wadsleyite.

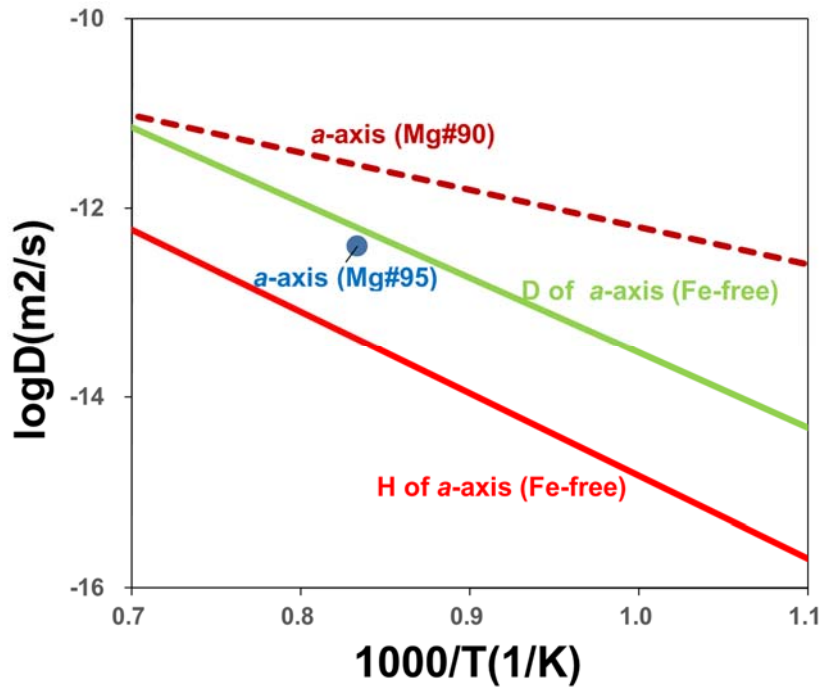


**Fig. 3.6.** Comparison of self-diffusivities normalized to  $a$ -axis between H(D) in Fe-bearing wadsleyite (Mg#90) (dark red line), H(D) in Fe-bearing wadsleyite (Mg#95) (blue point), H (red line) and D (green line) in Fe-free wadsleyite.

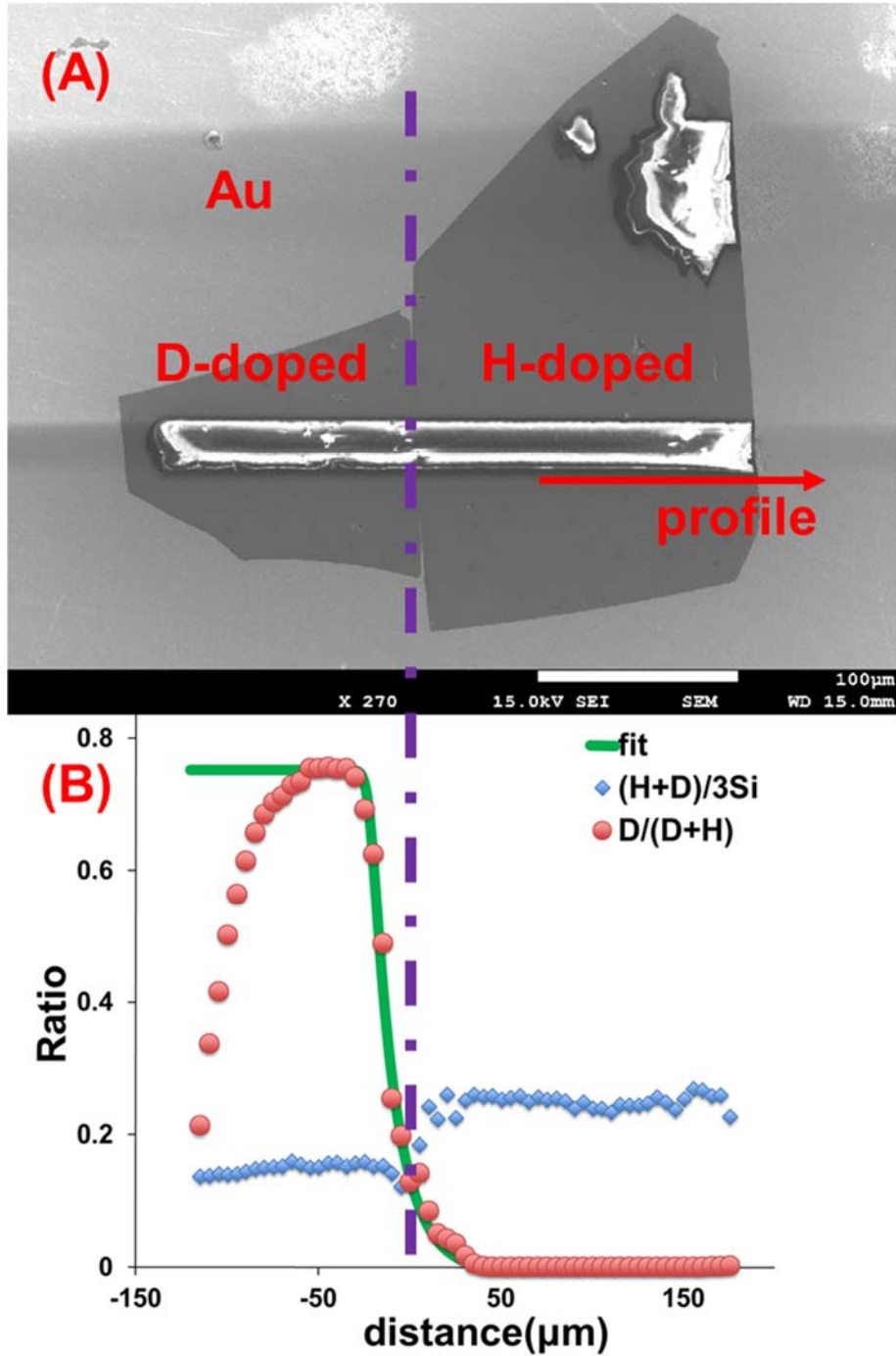


**Fig. 3.7.** An example of diffusion profile in Fe-free wadsleyite from Run. 1K2049 measured by SIMS. **(A)** SEM micrograph of sample showing array of craters from SIMS spot line analyses. **(B)** Diffusion profile from one crystal edge to another crystal edge perpendicular to the interface on the polished surface.

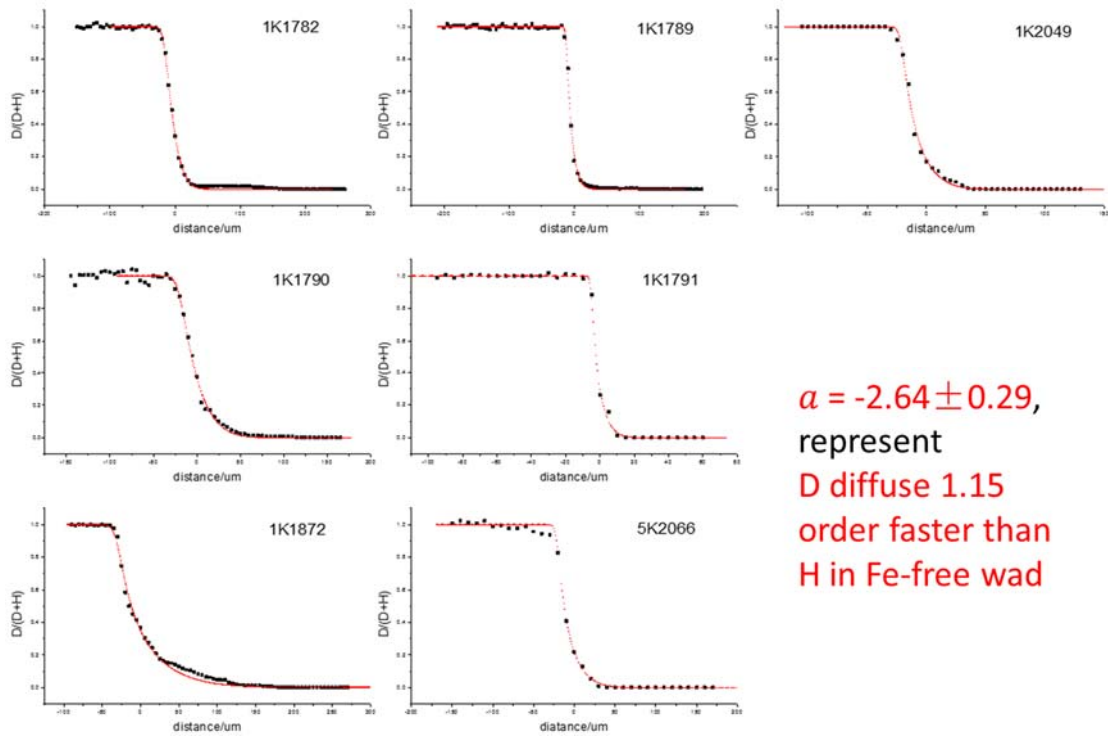


**Fig. 3.8.** All diffusion profiles in Fe-free wadsleyite measured by SIMS and fitted by Fortran step-by-step simulation.

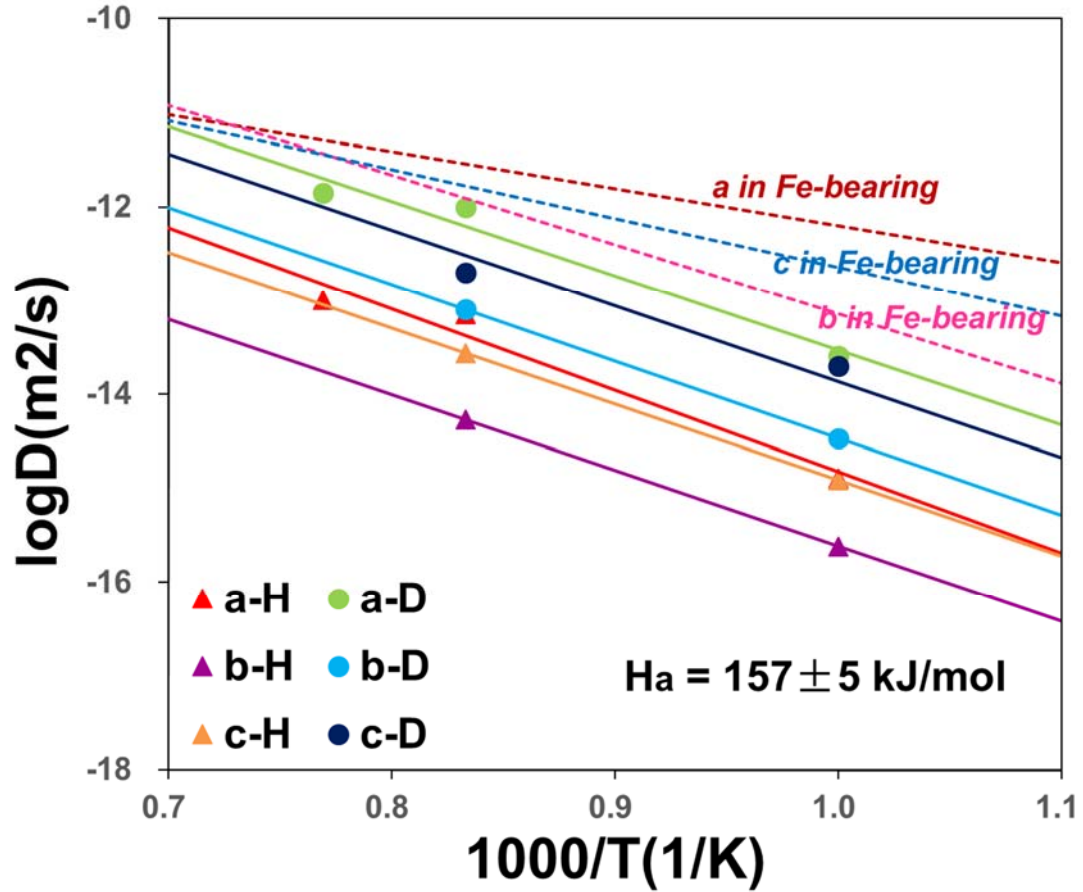


**Fig. 3.9.** Arrhenius plot of hydrogen and deuterium self-diffusion in Fe-free wadsleyite and comparison with hydrogen (deuterium) self-diffusion in Fe-bearing wadsleyite (Mg#90). The upper three dashed lines represent the diffusivities obtained from Fe-bearing wadsleyite. The middle and under three lines are simulation results of deuterium and hydrogen self-diffusivities in Fe-free wadsleyite, respectively. For every group, different colors represent normalized to different typical orientations. The activation enthalpise  $H_a$  of hydrogen and deuterium self-diffusion in Fe-bearing wadsleyite with different typical orientations are similar,  $\sim 157$  kJ/mol.

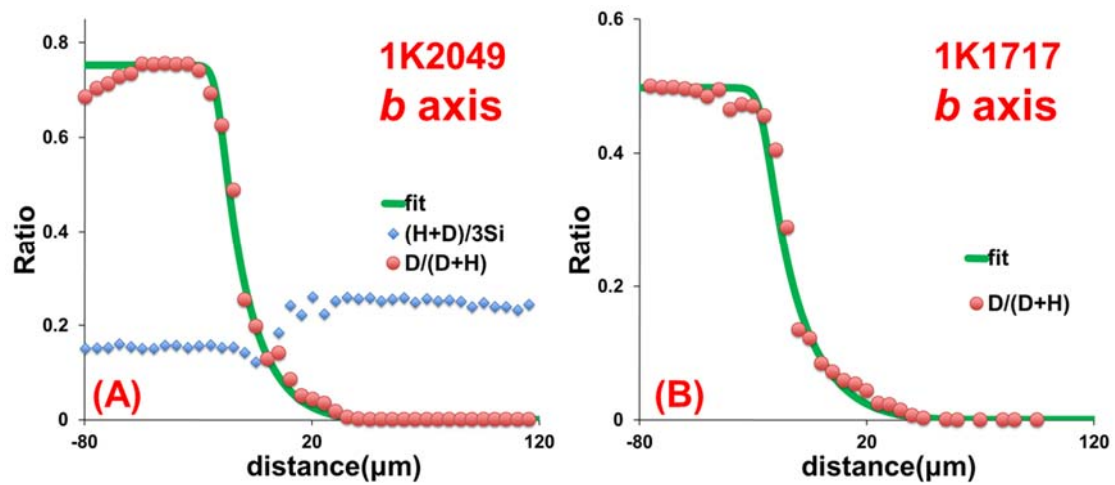


**Fig. 3.10.** Comparison of H-D inter-diffusion profiles in Fe-free wadsleyite at 1200 K between different crystal pairs from (A) 5K2141 and 1K1710 group and (B) 5K2033 and 5K2038 group. Though bulk water content in crystals from 5K2033 and 5K2038 are similar (**Table 2.2**), Run. 1K1717 revealed nearly same asymmetric property as Run. 1K2049.

## Chapter 4

### Discussions and implications

#### 4.1 Multiple hydrogen diffusion mechanism

##### 4.1.1 Hydrogen migration along interstitial sites

Statistical mechanics diffusion (random walk) function suggests that diffusion coefficient of species  $i$  ( $D_i$ ) is largely influenced by points defect condition (*Shewmon*, 1989):

$$D_i = Ax_v\Gamma_i \quad (4.1)$$

where  $A$  is empirical constant,  $x_v$  is the fraction of vacant, namely, sum concentration of unfilled and partially-filled defects and  $\Gamma_i$  is the probability of atom  $i$  jump when the neighboring site is partly-filled or empty. For hydrogen migration along Mg defects, the concentration of unfilled  $V''_{Mg}$  and partially-filled  $H'_{Mg}$  defects in Fe-free wadsleyite are extremely low ( $\sim 10^{-12}$ , *Verma and Karki*, 2009). In Fe-bearing wadsleyite, the concentration of effective vacant for hydrogen jumping would significantly augment according to the charge equilibrium with  $Fe_{Mg}^{\cdot}$ . Thus as **Fig. 4.1** showed, in Fe-free condition, since low concentration of vacant for jumping cruelly stagnates hydrogen self-diffusivities along Mg defects, we might observe another diffusion mechanism which is concealed in Fe-bearing condition and substantially irrelevant with Fe content, for examples, hydrogen diffusion along interstitial sites or Si defects.

As for effective defects in bulk diffusion, the mechanism allows either higher

hydrogen concentration or higher self-diffusivity than hydrogen diffusion along Mg defects. Si defects can be excluded because the previous study on neutron powder diffraction of hydrous wadsleyite demonstrated that dominant concentration of hydrogen (D) accommodate in M3 sites [*Sano-Furukawa et al.*, 2011] and both hydrogen diffusion experiments and ab initio simulations suggested lower mobility of hydrogen in Si and O sites [*Shimojuku et al.*, 2009, *Verma and Karki*, 2009, *Padrón-Navarta et al.*, 2014]. Although concentration of interstitial proton in wadsleyite is relatively low, free proton mobility could be much larger than hydrogen along Mg defects [*Verma and Karki*, 2009] and seems to be the sole candidate for the new mechanism observed in Fe-free wadsleyite. It is extreme lack of experimental proof about interstitial proton diffusion mechanism before present study though there has been theoretical model [*Karato*, 2013] and simulation support [*Verma and Karki*, 2009]. Our results provided strong evidence of multiple hydrogen diffusion species in wadsleyite.

#### **4.1.2 Evolution of asymmetry in Fe-free condition**

In multiple hydrogen mechanism, there are three types of hydrogen migration: (1) along Mg defects (2) along interstitial sites and (3) from Mg sites to interstitial sites. Based on Boltzmann distribution expression, jumping probability  $\Gamma_i$  usually functions to migration energy  $E_i$  and temperature:

$$\Gamma_i = A * \exp\left(\frac{-E_i}{RT}\right) \quad (4.2)$$

Thus, at a given temperature, the difference of jumping or diffusion probabilities between hydrogen isotopes is inverse proportion to absolute difference of migration

energy.

$$\frac{\Gamma_D}{\Gamma_H} = \exp\left(\frac{E_H - E_D}{RT}\right) = \exp(2.64) \approx 14, \text{ namely, } E_H - E_D \approx 22 \text{ kJ/mol} \quad (4.3)$$

Asymmetry factor calculated from our experiments is  $\sim -2.64$ , representing that deuterium diffuses about 14 times faster than hydrogen in Fe-free wadsleyite. In migration types (1) and (2), to product 14 times difference between diffusivities, it needs the migration energy for deuterium is  $\sim 22$  kJ/mol smaller than that for hydrogen at 1000 K (**Eq. 4.3**). Considering relative smaller migration barrier,  $<150$  kJ/mol referred from former [e.g., *Kohlstedt and Mackwell, 1998; Demouchy and Mackwell, 2003; Dufrane and Tyburczy, 2012; Karato, 2013; Yoshino et al., 2013*] and present studies for migration along Mg defects and  $<80$  kJ/mol referred from ab initio calculation [*Verma and Karki, 2009*] for migration along interstitial sites, respectively, 22 kJ/mol is amplified and leads to unreasonable large difference in proportion between hydrogen isotopes, 15% and 22% in migration types (1) and (2), respectively. Thus there is no expectation on large difference between hydrogen and deuterium self-diffusivities along either interstitial sites or Mg defects. In migration type (3), the differences between hydrogen isotopes of jump possibilities from Mg sites to interstitial sites could diversify the isotopes fraction in interstitial sites from bulk isotopes concentration to produce profound asymmetric properties. Smaller absolute differences of migration barrier between hydrogen and deuterium,  $\sim 11$  kJ/mol could explain observed asymmetry factor,  $-2.64$  in Fe-free wadsleyite as **Eq. 4.4** showed (demonstrated in later simulation parts).

$$\frac{\Gamma_D}{\Gamma_H} = \exp\left(\frac{E_H - E_D}{RT}\right) = \sqrt{\exp(2.64)} \approx 3.7, \text{ namely, } E_H - E_D \approx 11 \text{ kJ/mol} \quad (4.4)$$

On the other hand, ab initio simulation concluded relative large barrier energy, ~250 kJ/mol for hydrogen jumping from Mg site to interstitial site [Verma and Karki, 2009]. Thus ~4% energy difference required in proportion suggests distinguish jumping possibilities from Mg sites to interstitial sites between hydrogen isotopes might be the logical origin which lead to significant asymmetry in H-D inter-diffusion profiles.

Since stoichiometry must be preserved in H-D inter-diffusion process [Karato, 2013], the ratio  $k$  between total water concentration in interstitial sites,  $C_{H+D}^{in}$  and bulk water content,  $C_{H+D}^{bulk}$  must be fixed at arbitrary profile position  $x$  and duration  $t$ . The local equilibrium condition between hydrogen isotopes accommodated in interstitial sites and Mg defects can be expressed:

$$C_{D(x,t)}^{in} = \frac{P_D C_{D(x,t)}^{bulk}}{P_D C_{D(x,t)}^{bulk} + P_H C_{H(x,t)}^{bulk}} \times k C_{H+D}^{bulk} \quad (4.5)$$

$$C_{H(x,t)}^{in} = \frac{P_H C_{H(x,t)}^{bulk}}{P_D C_{D(x,t)}^{bulk} + P_H C_{H(x,t)}^{bulk}} \times k C_{H+D}^{bulk} \quad (4.6)$$

where  $C_{D(x,t)}^{in}$ ,  $C_{H(x,t)}^{in}$ ,  $C_{D(x,t)}^{bulk}$  and  $C_{H(x,t)}^{bulk}$  are the deuterium and hydrogen concentrations in interstitial sites and bulk concentrations, respectively.  $P_D$  and  $P_H$  are the jump probabilities from a Mg site to an interstitial site for deuterium and hydrogen (deuterium and hydrogen concentrations in Mg sites are approximately equal to bulk ones), respectively. If the  $P_D$  is not equal to  $P_H$ , the isotopic gradient in interstitial sites is different from bulk isotopic gradient.

Karato [2013] put forward a theoretical inter-diffusion model for multiple hydrogen species characterized by dividing single diffusion step into two stages: (1) isotope jump and (2) local exchange. At arbitrary profile position  $x$  and duration  $t$ , local equilibrium conditions from Eq. 4.5 and 4.6 suggest that there are same isotopic

fractions in interstitial sites and Mg defects when  $P_D = P_H$  (**Fig. 4.2A**). At first stage, when multiple species are present, concentration gradient must be present for each species that varies as a function of position. Consequently, each species will diffuse driven by the concentration gradient, and the diffusion flux should be proportional to the diffusion coefficient of each species. Thus at duration  $t + \delta t_{iso}$ , isotope fraction variations in interstitial sites is larger than ones in Mg defects because of higher self-diffusivities along interstitial sites, leading to breakdown of local isotopic equilibrium between each species (**Fig. 4.2A**). It must cause a H-D exchange between local interstitial sites and Mg sites in following stage (2). At duration  $t + \delta t_{iso} + \delta t_{loc}$ , the new isotopic equilibrium is reconstructed (**Fig. 4.2A**) and H-D inter-diffusion turns into next single step. Based on *Karato (2013)*'s calculation,  $\delta t_{iso}$  is much larger than  $\delta t_{loc}$  and it means that local equilibrium must be well achieved during an isotope diffusion experiment.

$$\frac{\delta t_{iso}}{\delta t_{loc}} \approx \left(\frac{l}{a}\right)^2 \gg 1 \quad (4.7)$$

where  $l$  is the diffusion length in  $\mu\text{m}$  unit and  $a$  is the distance between hydrogen atoms in nm unit.

However, in the present study where  $P_D$  might not be equal to  $P_H$ , local isotopic equilibrium achieving to the bulk isotopic fraction and isotopic gradient in interstitial sites is always different from bulk isotopic gradient (**Fig. 4.2B**). Developing from *Karato (2013)*'s model, a coupled-diffusion model was constructed by introducing interstitial proton mechanism in addition to diffusion mechanism in Mg sites and distinguish jump probabilities from Mg site to interstitial site for

hydrogen and deuterium (**Fig. 4.3**). The simulation results reveal that bulk hydrogen diffusion profile feature is mostly controlled by ratio  $R = \frac{C_{H+D}^{in} D_{self}^{in}}{C_{H+D}^{Mg} D_{self}^{Mg}}$  and insensitive to asymmetric factor  $A = \frac{P_D}{P_H}$  except at high  $R$  value ( $> 5$ ), where  $C_{H+D}^{in}$  and  $C_{H+D}^{Mg}$  are bulk hydrogen concentrations in interstitial and Mg sites, respectively,  $D_{self}^{in}$  and  $D_{self}^{Mg}$  are hydrogen self-diffusivities along interstitial sites and Mg defects, respectively. If  $R > 1$ , free proton migration along interstitial sites controls the diffusion process and if  $R < 1$ , dominant kinetics mechanism is diffusion along Mg defects. In Fe-bearing (Mg#90) wadsleyite, hydrogen diffusion along Mg defects dominates the kinetics process and inter-diffusion profiles are symmetric (**Fig. 3.3 and 4.3E**). In wadsleyite (Mg#95), partially-filled  $H'_{Mg}$  concentration decreases and  $R$  value increases ( $\sim 1$ ), the resultant H-D inter-diffusion is determined by both migration mechanisms. At  $R < 5$ , asymmetric profile is not comparable and consistent with inconspicuous asymmetry obtained from wadsleyite with low Fe content (**Fig. 3.5 and 4.3C**). Asymmetric profiles are observed evidently in Fe-free condition since interstitial proton migration controls the diffusion process correspond to decrease of  $D_{self}^{Mg}$  to more forward (**Fig. 3.8 and 4.3A**). In Fe-free condition, profile diffusion coefficients at H-doped and D-doped infinite end are  $AD_{self}^{in}$  and  $\frac{D_{self}^{in}}{A}$ , respectively, indicating asymmetric factor obtained from empirical **Eq. 3.6** equal to  $\ln(A^2)$ . The different magnitudes and anisotropies in H-D inter-diffusion between Fe-free and Fe-bearing wadsleyite are owing to the different dominant migration mechanisms adjusting to the vacant concentration ( $V''_{Mg}$  plus  $H'_{Mg}$ ).

#### 4.1.3 Comparison with Karato (2013)'s model

Because of low ferric iron solubility in olivine, present multiple hydrogen model predicts observation of transformation of dominant hydrogen diffusion mechanism as temperature increases, which has been reported by recent electrical conduction experiments on hydrous olivine single crystals [Dai and Karato, 2014]. However, the present model suggests at high temperature, diffusion or proton conduction are controlled by free proton migration while at low temperature, hydrogen diffusion along Mg defects dominates the kinetics process, which is opposite to the Karato (2013)'s model. Regarding Arrhenius plot fitting is based on bulk water content no matter which mechanisms dominate the diffusion process, the obtained activation enthalpy should be controlled by both (1) temperature dependence of hydrogen self-diffusion along interstitial sites and (2) variation of concentration of interstitial proton as temperature when migration of free proton dominates the diffusion process.

$$\sigma_{EC} = C_H^{bulk} * k_{(T,P)} * \frac{D_{self}^{in} q^2}{K_b T} \quad (4.8)$$

where  $\sigma_{EC}$  is measured proton conductivity,  $C_H^{bulk}$  is bulk hydrogen concentration,  $q$  is charge,  $K_b$  is the Boltzmann constant,  $T$  is absolute temperature and  $k$  is the ratio  $k$  between total water concentration in interstitial sites and bulk water content.  $k$  also has temperature-dependence and direct evidence is that free proton never been detected at room temperature in olivine and its high pressure polymorphs. Although ab initio simulation concluded lower activation enthalpy for free proton migration than diffusion along Mg defects, sum of enthalpy (1) and (2) might be larger than enthalpy for hydrogen diffusion along Mg sites and the mechanism transformation observed at high temperature mainly attributes to increasing concentration of

interstitial proton. On the other hand, multiple hydrogen mechanism would also contribute effectively to H-D differentiation in the upper mantle, where  $Fe^{3+}/\Sigma Fe$  is relative low,  $\sim 3\%$  [O'Neill *et al.*, 1993; McCammon *et al.*, 2004]. Observed depleted- $\delta D$  in NAMs from xenolith [Bell and Ihinger, 2000] might ascribe to kinetic fractionation in dehydration during magma rising.

## 4.2 Implication to water distribution in the transition zone

### 4.2.1 Bulk hydrogen diffusivities in the transition zone

Hydrogen diffusivities in Fe-bearing wadsleyite polycrystals have been first reported by Hae *et al.* [2006]. Based the expression proposed by Balluffi *et al.* [2005],

$$D_H^{eff} = D_H^L + \left(\frac{3\delta}{d}\right)D_H^{gb} \quad (4.9)$$

where  $D_H^{eff}$ ,  $D_H^L$  and  $D_H^{gb}$  are hydrogen diffusivities for bulk, lattice and grain boundary, respectively.  $d$  is the grain size,  $9 \mu m$  for wadsleyite aggregates from Hae *et al.* [2006] and  $\delta$  is the grain boundaries width. Imaging of grain boundaries using transmission electronic microscopy permitted the measurement of grain boundaries widths and to date is considered to be  $0.75 \text{ nm}$  (two monoatomic layers) (Hiraga and Kohlstedt, 2007, 2009). Comprehend with present average self-diffusion coefficient, hydrogen grain boundary diffusivities in Fe-bearing wadsleyite can be estimated as follows (Fig. 4.4).

$$D_H^{gb} = 10^{-3.25} * \exp\left(\frac{125 \text{ kJ/mol}}{2.303*RT}\right) \text{ m}^2/\text{s} \quad (4.10)$$

At the transition zone condition, hydrogen grain boundary diffusivities are  $\sim 2$  orders of magnitude higher than lattice diffusivities. Grain sizes in normal mantle

transition zone might be relatively large ( $>100 \mu\text{m}$ ) and lattice diffusion might be dominant for hydrogen transportation (**Fig. 4.5**). Due to grain size reduction during phase transformation under stress condition [Rubie and Brearley, 1990; Ito and Sato, 1991; Riedel and Karato, 1997], grain boundary mechanism might control the hydrogen migration in the subduction zone. However, considering relative low temperature conditions expected from the subduction zone, the hydrogen diffusivities  $D_H^{\text{eff}}$  in the mantle transition zone is estimated to be lower than -9 log units of  $\text{m}^2/\text{s}$  (**Fig. 4.5**). Note that the present result yielding self-diffusion cannot be simply compared with the results from Hae *et al.* [2006] because the former study determined diffusion diffusivities of hydrogenation. However, currently available data is limited. In addition, the calculated grain boundary diffusion coefficient is similar to that obtained from olivine [Demouchy, 2010]. Therefore, the present results will be applied to hydrogenation process in the following discussion.

#### 4.2.2 Water heterogeneity in the transition zone

Assuming upper limit of  $D_H^{\text{eff}}$  in the mantle transition zone is -9 log units of  $\text{m}^2/\text{s}$ , we can estimate the characteristic hydrogen diffusion distance in the mantle transition zone at a given duration using the following equation [Crank, 1979]:

$$x = \sqrt{D_H^{\text{eff}} t} \quad (4.11)$$

where  $x$  is the characteristic distance in meter and  $t$  is the duration in second. The characteristic distance for hydrogen diffusion is found to be  $\sim 1.8 \text{ km}$  after 100 Myr, leading to the heterogeneity of water distribution in the mantle transition zone estimated from the electrical conductivity and seismic velocity [Hae *et al.*, 2006; Mao

*et al.*, 2012; *Yoshino and Katsura*, 2013].

The time scale of water heterogeneity persistence in the transition zone is also discussed assuming a spherical geometry with diameter  $d$ . The boundary condition is a constant normalized concentration of 1 at the surface of the sphere, representing a new equilibrium concentration. The initial condition is a normalized concentration  $C_0 = 0$  throughout the sphere. The appropriate solution for the concentration at the center of the sphere is given [*Crank*, 1979]:

$$C_{(t)} = 1 + 2 \sum_1^n (-1)^n \exp\left(-\frac{D_H^{eff} n^2 \pi^2}{d^2}\right) \quad (4.12)$$

where  $C_{(t)}$  is normalized concentration,  $d$  is the radius of the sphere, and  $D_H^{eff}$  is estimated to upper limit in the transition zone,  $-9 \log$  units of  $m^2/s$  from present study.

In **Fig. 4.6**, the equilibration time of a heterogeneity with a certain diameter  $d$  is shown in a log-log plot. The equilibration time  $t_{0.95}$  is defined as the time needed to equilibrate the grain to such an extent that the normalized concentration at the center is 0.95. **Fig. 4.6** shows that on experimental timescales of 1 hour, equilibrium can only be achieved on the scale of a few millimeters. For heterogeneity with a diameter of several meter, equilibrate on timescales equivalent to a human lifetime or longer. During a timescale of the typical subduction slab age, assumed to be 50-200 Myr [*Mosenfelder et al.*, 2001], the size of a heterogeneity completely re-equilibrating would be tiny, less than 1 km (**Fig. 4.6**), comparing with heterogeneity scales observed in wedge mantle by geophysics technical such as magneto-telluric (MT) and seismic velocity methods [e.g., *Fukao et al.*, 2004; *Ichiki et al.*, 2006; *Kelbert et al.*, 2009; *Baba et al.*, 2010].

### 4.2.3 Long-term preserved supercritical fluid in wedge mantle

Low mobility of hydrogen in transition zone condition suggests water heterogeneity in subduction slabs can be long-term preserved and hydration of surrounding dry mantle is not so effective. On the other hand, thermal diffusivities are  $\sim 3$  orders magnitudes larger than hydrogen diffusivities [Xu *et al.*, 2004] in the transition zone condition, leading to temperature homogenization between wedge and surrounding mantle is more rapid. Thus maximum water solubility in wet slab wadsleyite and ringwoodite decrease sharply during slab water sluggish diffusion out to dry surrounding mantle. Consequently, supercritical fluid might occur and long-term preserve in some range of mantle transition zone, for example, at top of the stagnant slab, rich in water because of decomposition of phase A [Ohtani *et al.*, 2003, 2004] when the maximum water solubility lower than bulk water content.

Based on above coupled-diffusion mechanism, we have simulated the evolution of supercritical fluid at the interface between stagnant slab and surrounding mantle to investigate the possibility and locality of fluid in the wedge mantle. Initial condition for surround mantle is well constrained by former [Katsura *et al.*, 2010; Yoshino and Katsura, 2013] and present studies, assuming to 0.1 wt.% water content and 1900 K. Simulation were performed on various initial slab temperatures, 1000-1600 K and water contents, 1-2.5 wt.% to determine the function between initial slab temperatures and the minimum initial water contents to generate supercritical fluids. Log thermal and hydrogen diffusivities are -6 and -9  $\text{m}^2/\text{s}$  referred from Xu *et al.* [2004] and present study, respectively. The temperature dependence of the maximum water

solubility in wadsleyite was calculated based on the expression from *Kohlstedt et al.* [1996] (**Fig. 4.7**):

$$C_{max} = 0.079wt. \% * \exp\left(\frac{39kJ/mol}{RT}\right) \quad (4.13)$$

Our results demonstrated that amount of water might exsolve from minerals to generate supercritical fluids at the top of stagnant slabs according to sluggish water homogenization process although water content in the slabs is much lower than maximum water solubility at the beginning (**Fig. 4.8**). After fluids generation, it could be constrained within a narrow range and long-term preserved after more than 100 Myr, a typical slab age, at the top of the stagnant slabs (**Fig. 4.9**).

### 4.3 Implications for electrical conduction

Electrical conductivity of mantle minerals is generally controlled by a combination of ionic conduction ( $\sigma_i$ ), hopping of electron holes between ferrous and ferric iron ( $\sigma_h$ ), and migration of protons ( $\sigma_p$ ). At wet condition, proton conductivity is usually orders magnitude higher than the others and dominates the bulk conductivity at low temperatures. If we consider the general case, the bulk conductivity is expressed by

$$\sigma = \sigma_i + \sigma_h + \sigma_p \quad (4.14)$$

In this study, proton conductivities from hydrogen self-diffusion coefficients in Fe-bearing wadsleyite and ringwoodite were calculated based on the Nernst-Einstein relation,

$$\sigma_p = \frac{D_H C_H q^2}{K_b T} \quad (4.15)$$

where  $D_H$  is the hydrogen self-diffusion coefficient,  $C_H$  is concentration of hydrogen,  $q$  is charge,  $K_b$  is the Boltzmann constant, and  $T$  is absolute temperature. Bulk conductivities are summation of all conduction processes based on **Eq. 4.14**. To estimate the bulk conductivity of wadsleyite and ringwoodite, ionic and hopping conduction of wadsleyite and ringwoodite were taken from those of dry wadsleyite and ringwoodite polycrystals of *Yoshino et al.* [2008]. *Huang et al.* [2005] determined only bulk conductivities for hydrous ringwoodite so that their proton conductivities by subtracting the dry data from *Yoshino et al.* [2008] were estimated.

#### **4.3.1 Electrical conductivity in Fe-bearing wadsleyite**

In Fe-bearing wadsleyite, proton conductivity estimated from hydrogen self-diffusion coefficients has similar magnitudes with data of *Yoshino et al.* [2008] at a wide range of water content and transition zone condition but ~1 order of magnitude lower than results from *Dai et al.* [2009] (**Fig. 4.10A**). It is indistinguishable between bulk conductivities obtained from this study and results of *Yoshino et al.* [2008] with a wide range of water content (**Fig. 4.10B** and **4.11A**). The activation enthalpy  $H_a$  of proton conduction of wadsleyite from these studies are similar, with value ~100 kJ/mol).

#### **4.3.2 Electrical conductivities in Fe-bearing ringwoodite**

In Fe-bearing ringwoodite, proton and bulk conductivities of ringwoodite with water content < 1000 ppmw are consistent with that measured by *Yoshino et al.* [2008] but ~2 orders of magnitude lower than *Huang et al.* [2005] (**Fig. 4.12**). At higher water content, the present results are lower than results from both *Yoshino et al.* [2008]

and *Huang et al.* [2005] conspicuously (**Fig. 4.11B**). *Yoshino et al.* [2008] observed a large reduction of  $H_a$  as water concentration in hydrous ringwoodite increases (**Fig. 4.12**), and introduced a term of water content dependence of  $H_a$  ( $\alpha C_{\text{H}_2\text{O}}^{\frac{1}{3}}$ ) to fit the conductivity data. However, in this study, the diffusion profiles in Fe-bearing ringwoodite revealed symmetrical characteristics (**Fig. 3.1**) although the total water contents in D-doped crystals are 30% lower than in H-doped ones (**Table 2.2**), suggesting an insignificant influence of water concentration on the activation enthalpy  $H_a$  for hydrogen self-diffusion. Because of its reduction with increasing water content, the activation enthalpy in hydrous ringwoodite from *Yoshino et al.* [2008] is lower than results from *Huang et al.* [2005] and this study at high water content (**Fig. 4.12**).

At high temperatures corresponding to the mantle transition zone, the other conduction mechanisms become dominant, since activation energy for small polaron conduction in Fe-bearing olivine and its high-pressure polymorphs are higher than that for proton conduction [*Yoshino*, 2010]. **Fig. 4.13** shows the bulk electrical conductivity of ringwoodite taking into consideration of the small polaron conduction. Small amount of water in ringwoodite insignificantly contributes to the conductivity due to large contribution of hopping conduction at the transition zone condition. Assuming that Mg# of ringwoodite is 90, even 1 wt.% H<sub>2</sub>O would only increase the electrical conductivity of ringwoodite of ~0.3 log unit.

### 4.3.3 Origin of discrepancy of proton conduction data

If supercritical fluid exists along the grain-boundaries, it is likely to establish three-dimensional interconnected network in finer grain-size samples during heating.

Generally direct measurements on finer grain-size samples would be affected more seriously by dehydration and yielded larger electrical conductivities. The present results estimated from lattice inter-diffusivities in Fe-bearing wadsleyite and ringwoodite agree better with results from *Yoshino et al.* [2008] possible due to relative larger grain size (100-500  $\mu\text{m}$ ) used in *Yoshino et al.* [2008] than those (5-10  $\mu\text{m}$ ) used in *Dai et al.* [2009] and *Huang et al.* [2005]. The discrepancy between electrical conductivity data from *Yoshino et al.* [2008] and this study on ringwoodite at high water content might also be in consequence of unavoidable dehydration.

#### **4.3.4 Estimation of water content in the transition zone**

Comparing electrical conductivity in hydrous wadsleyite and ringwoodite calculated from diffusion coefficient with the global average model by *Kelbert et al.* [2009], water content in the lower part of the transition zone is found to be less than 0.1 wt.% (**Fig. 4.11** and **4.14A**), which is consistent with Yoshino's model and recent studies using seismicity [*Mao et al.*, 2012]. In contrast, the hydrogen diffusion model cannot explain high conductivity anomalies beneath the Philippine Sea and northeastern China where descending slab stagnates at the transition zone (**4.14B**). In addition, it is difficult to explain these anomalies by hydration of wadsleyite and ringwoodite based on all the electrical conductivity databases because  $\sim 1$  wt.% water content in wadsleyite and ringwoodite leading to the higher conductivity [*Huang et al.*, 2005; *Yoshino and Katsura*, 2013] will largely decrease  $V_P$  and  $V_S$  [*Mao et al.*, 2012]. It is not consistent with seismic observations, which are characterized by higher  $V_P$  and  $V_S$  beneath the Philippine Sea and northeastern China compared to

values from Preliminary reference Earth model (PREM) (1.5 and 2% higher, respectively) [Fukao *et al.*, 2004]. These conductivity anomalies could attribute to variations in chemical composition (major or trace elements), oxidation state (oxygen fugacity level) and supercritical-fluids in some regions in or near stagnant slabs [Manthilake *et al.*, 2009; Yoshino *et al.*, 2009].

In reference to discussion in **section 4.2.3**, the presence of supercritical liquid can be proposed as the most possible explanation for the high conductivity in the wedge mantle. Melekhova *et al.* [2007] have shown that liquids in the MgO–SiO<sub>2</sub>–H<sub>2</sub>O system become supercritical above 11 GPa. The composition of the supercritical fluids coexisting with wadsleyite at 13.5 GPa and 1323 K is mainly H<sub>2</sub>O (60 wt.%) MgO (33 wt.%) and SiO<sub>2</sub> (7 wt.%) and H<sub>2</sub>O content slightly decreases with increasing temperatures (52 wt.% in 1523K). Considering significantly low temperature in the subduction zone compared to the normal mantle geotherm, the composition of supercritical fluids should be dominated by H<sub>2</sub>O [Melekhova *et al.*, 2007], which is significantly different from hydrous melts in terms of H<sub>2</sub>O content [Demouchy *et al.*, 2005]. Electrical conductivity measurements of supercritical H<sub>2</sub>O based on shock experiments at 15 GPa and 1273 K yielded a conductivity of around 100 S/m (Mitchell and Nellis, 1982), which is ~4 orders of magnitude higher than conductivities in hydrous wadsleyite with 1 wt.% water content at the same condition. If supercritical fluids coexist with hydrous wadsleyite (without hydrous phase), tiny fraction of supercritical fluids can govern bulk conductivity of rocks. As a first approximation, a 0.1% volume fraction can duplicate the observed 0.1 S/m

conductivity in the wedge mantle.

On the other hand, the effect of supercritical fluids on  $V_p$  and  $V_s$  under transition zone conditions might be negligible because of tiny volume fraction,  $<0.1\%$  considering the liquid or melt fraction dependence of seismic wave velocities [Yoshino *et al.*, 2005]. Seismic velocity observed from hydrous wadsleyite coexist with supercritical fluids in the subduction zone is likely to be faster than that observed by global average model mainly depending on subduction zone geotherm. A tiny amount of supercritical fluid agrees with geophysical observations including both high electrical conductivities and seismic velocities in the stagnant mantle.

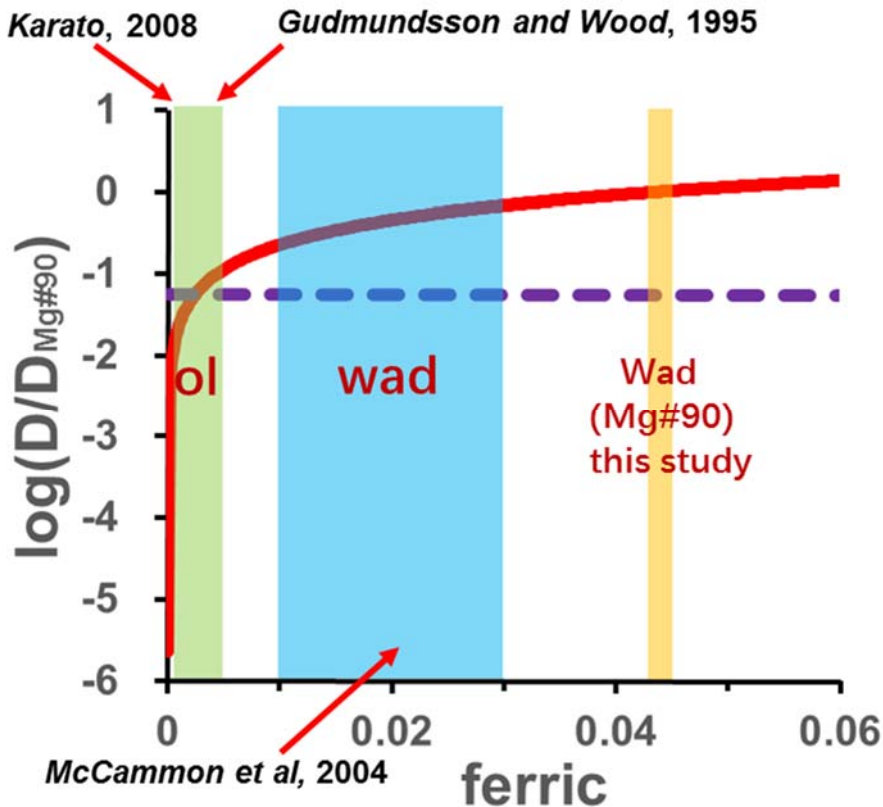


**Fig. 4.1.** Variation of hydrogen self-diffusivities along Mg defects at 1000 K as a function to the Ferric Fe concentration normalized to Mg sites displayed by red curve. Green range represents ferric concentration in mantle olivine. The upper and lower limits for olivine are referred from *Gudmundsson and Wood* [1995] and *Karato* [2008]. Wadsleyite in the transition zone estimated by *McCammon et al.* [2004] within blue range has higher ferric Fe concentration than olivine. Ferric Fe concentration in our Fe-bearing wadsleyite (Mg#90, yellow range) assumed equal to sample SZ0005 from *McCammon et al.* [2004], which were synthesized in nearly same condition as ours. Vertical axis means the log diffusivities normalized to the diffusivity from present wadsleyite (Mg#90) at 1000 K. The purple dashed line represents another hydrogen diffusion mechanism which do not migrate along Mg defects, which might control the diffusion process in Fe-free condition because of stagnation of hydrogen diffusion along Mg defects.

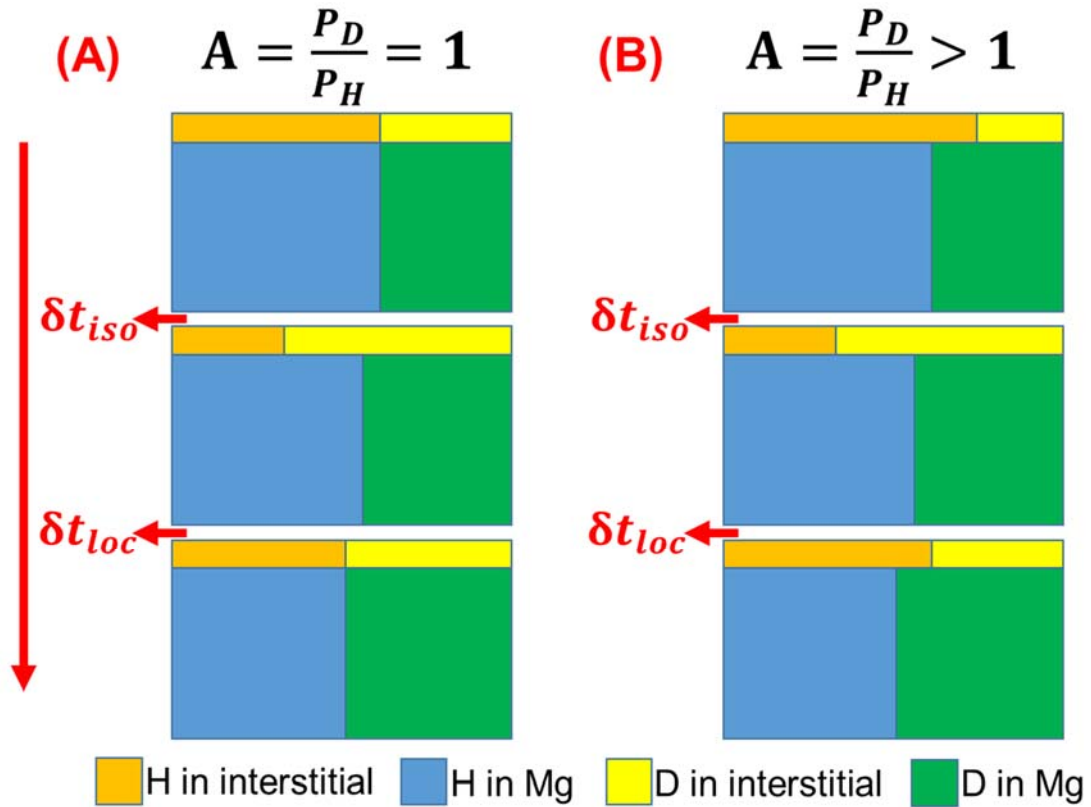


**Fig. 4.2.** Schematic drawings of two-steps H-D inter-diffusion model associate with interstitial free proton (A) assuming same jumping probabilities from Mg to interstitial sites between hydrogen isotopes from *Karato* [2013] and (B) assuming higher jumping probabilities of deuterium developed for present asymmetric observation. Different colors represent multiple hydrogen or deuterium species and square volumes represent specie fractions.

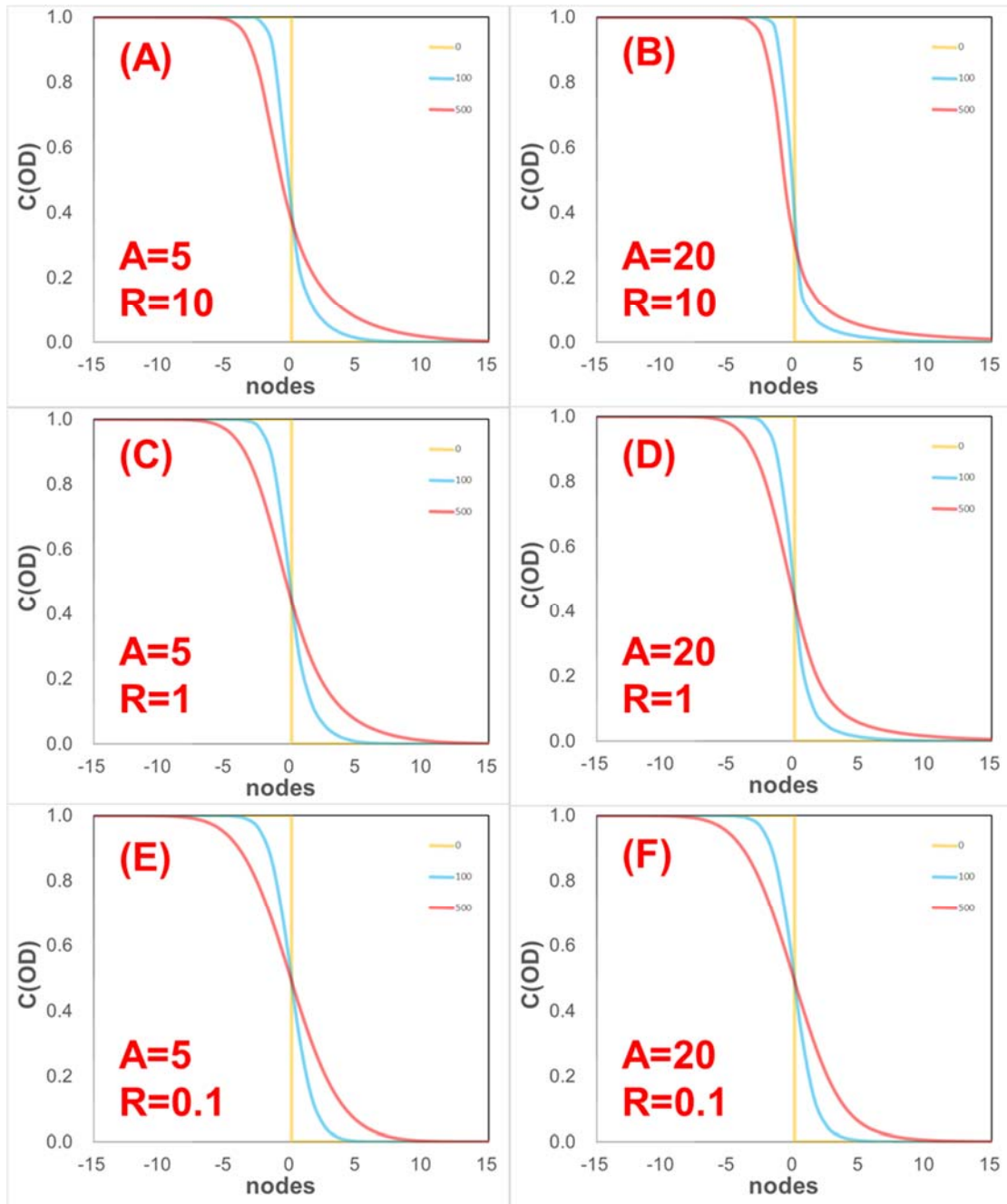


**Fig. 4.3.** Comparison of simulated profiles based on coupled-diffusion mechanism with various  $A$  and  $R$  values. Vertical axis indicates bulk deuterium fraction and horizontal axis shows nodes and indicate profile position. Bulk diffusivities are same for all profiles. Yellow curves show initial conditions with  $C(OD) = 0$  at  $x \geq 0$  and  $C(OD) = 1$  at  $x < 0$ . Blue and red curves represent diffusion profiles after 100 and 500 simulation steps, respectively, which mean duration.

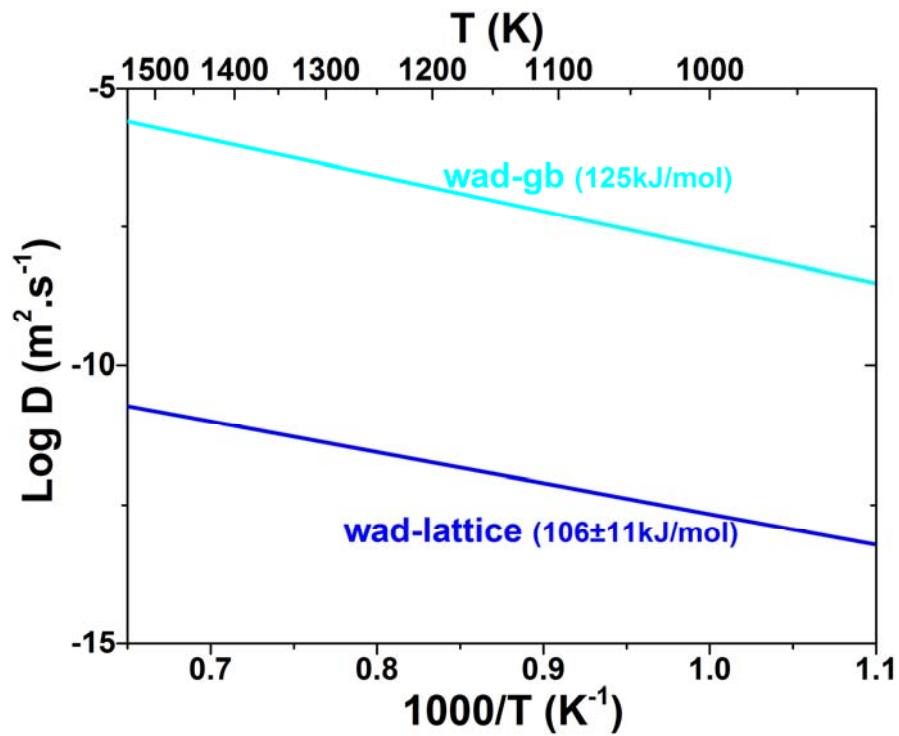


**Fig. 4.4.** Arrhenius plot of hydrogen grain-boundary diffusion and comparison with hydrogen lattice diffusion in Fe-bearing wadsleyite. Light blue line shows hydrogen grain boundary diffusivities in Fe-bearing wadsleyite with  $H_a = 125$  kJ/mol and  $D_0 = 10^{-3.25}$  m<sup>2</sup>/s. Dark blue line shows the geometric mean of hydrogen self-diffusivities of three orientations in Fe-bearing wadsleyite of this study at 16 GPa with  $H_a = 106 \pm 11$  kJ/mol and  $D_0 = 10^{-7.15 \pm 0.46}$  m<sup>2</sup>/s.

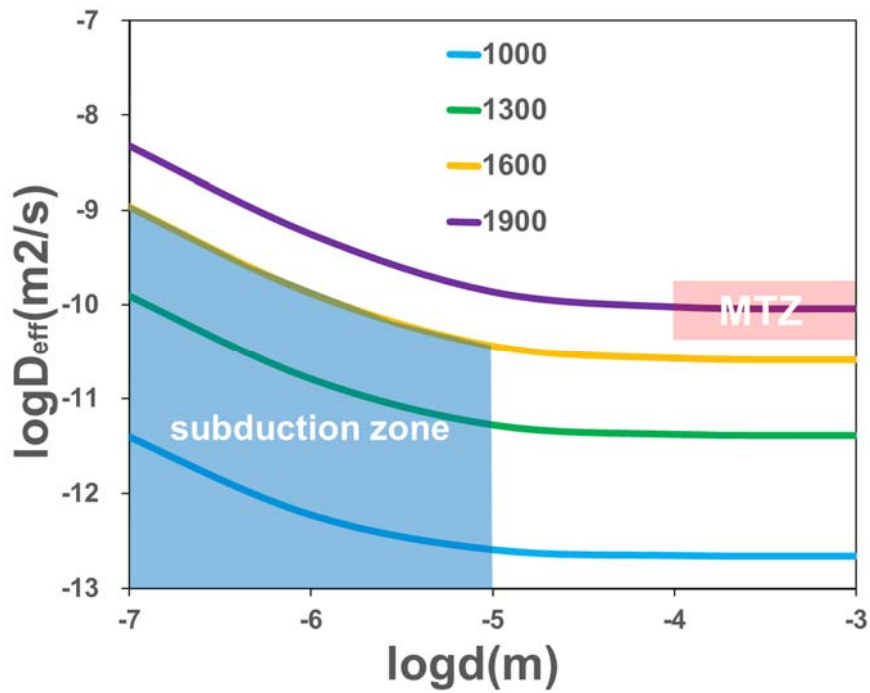


**Fig. 4.5.** Effect of the grain size,  $d$  on the hydrogen effective diffusion,  $D_{\text{H}}^{\text{eff}}$  in wadsleyite, at different temperatures for a polycrystalline aggregate of wadsleyite. The different color lines are calculated using **Eq. 4.9** at different temperatures. Right red region denotes normal mantle transition zone condition derived from *Katsura et al.* [2010] with large grain size  $>100 \mu\text{m}$ . Left blue region indicates bulk hydrogen diffusivities in subduction zone characterized by lower geotherm and smaller grain size ( $<1 \mu\text{m}$ ).

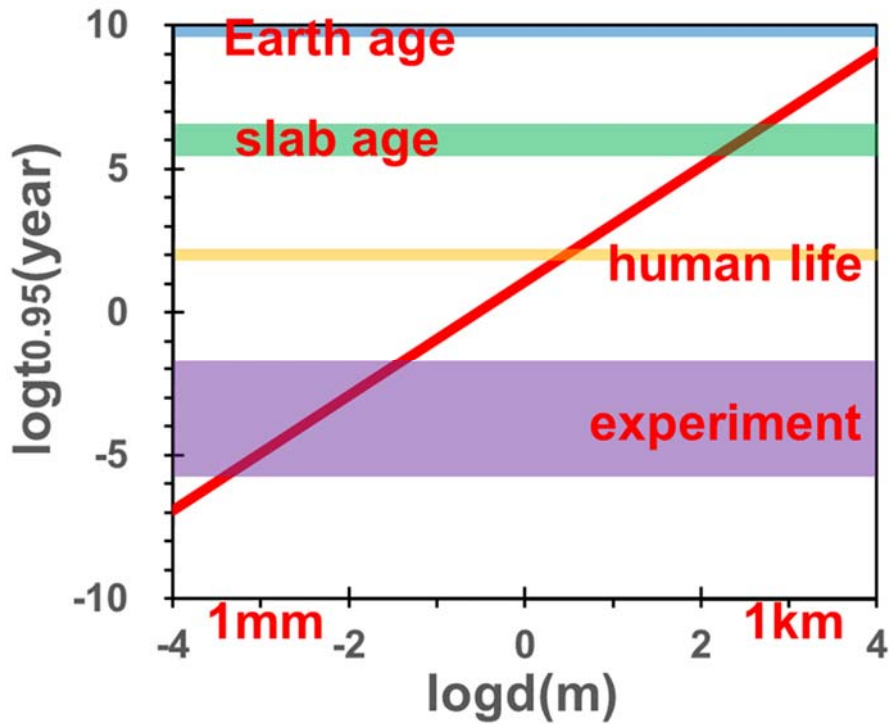


**Fig. 4.6.** Equilibration times  $t_{0.95}$  as a function of the size of a chemical heterogeneity using the effective hydrogen diffusion coefficient assuming to  $10^{-9} \text{ m}^2/\text{s}$  in the transition zone. The heterogeneity is assumed to have the form of a sphere with diameter  $d$ . Also shown are experimental timescales (purple range), the average human lifetime (yellow range), the typical subduction slab ages (green range) and the age of the Earth (blue range).

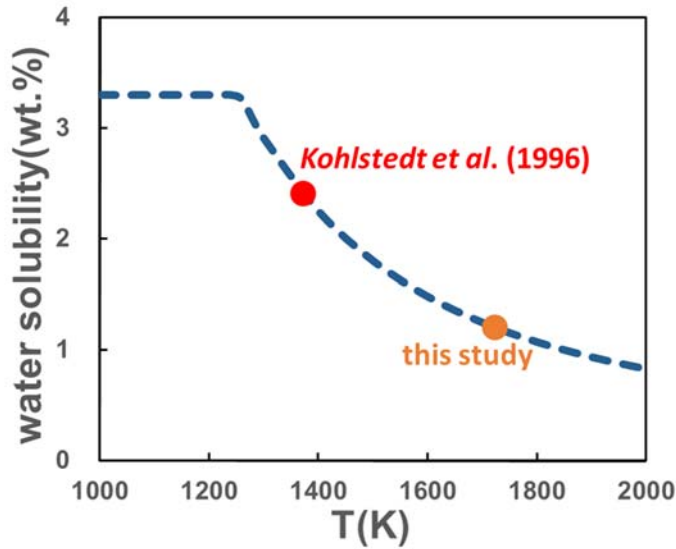


**Fig. 4.7.** Calculated temperature dependence of the maximum water solubility in wadsleyite. The solubility curve was calculated based on experimental data from *Kohlstedt et al.* [1996] (red point) and present study (yellow point). At low temperatures from 1000-1300 K, water solubility in wadsleyite is constrained by crystal structure limit, 3.3 wt.% [*Smyth*, 1994].

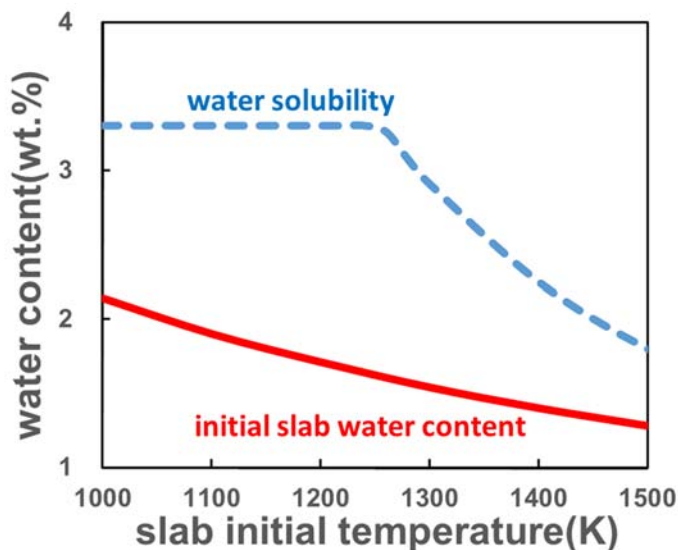


**Fig. 4.8.** The minimum initial slab water content required to generate supercritical fluids in the stagnant slabs as a function to the initial slab temperatures (red solid curve), which is much lower than maximum water solubility (blue dashed curve).

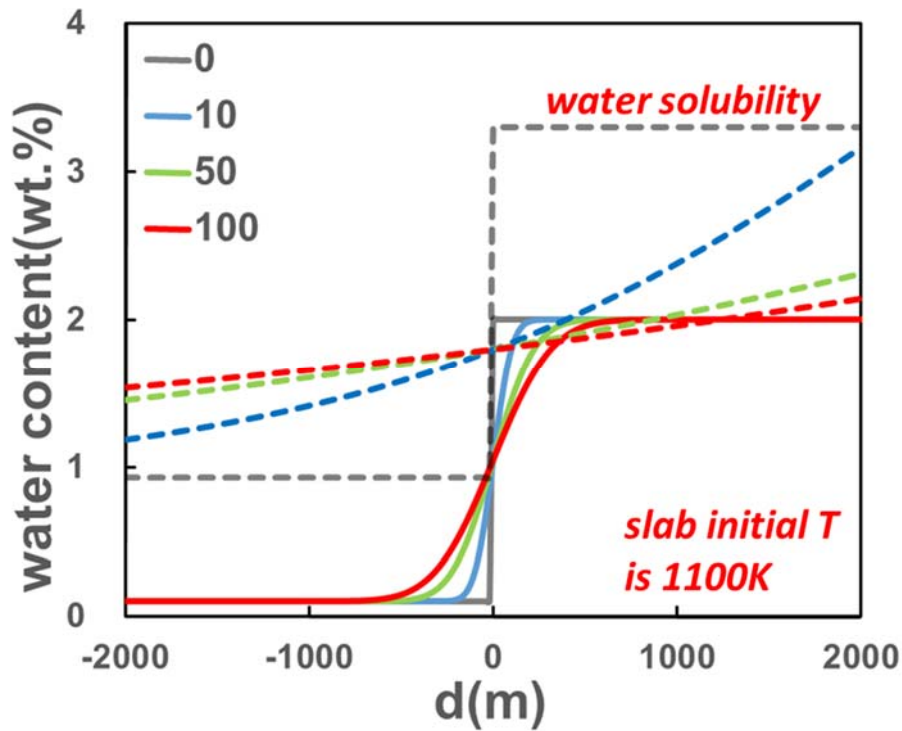


**Fig. 4.9.** An example of coupled-diffusion profiles at the junction part between stagnant slab and surrounding mantle with initial slab temperature, 1100 K and water content, 2 wt.% function to the diffusion length  $d$  and duration. Different colors mean increasing time scales from 0 to 100 Myr. The dashed curves represent maximum water solubility depending on thermal diffusion and solid curves represent water distribution along the diffusion length depending on hydrogen diffusion. The crossover between solid and dashed curves suggest water storage in the slab overflow the maximum water solubility at the moment and supercritical fluids occur. After fluids generation, crossover part is constrained within a narrow range at the top of stagnant slab and long-term preserved more than 100 Myr.

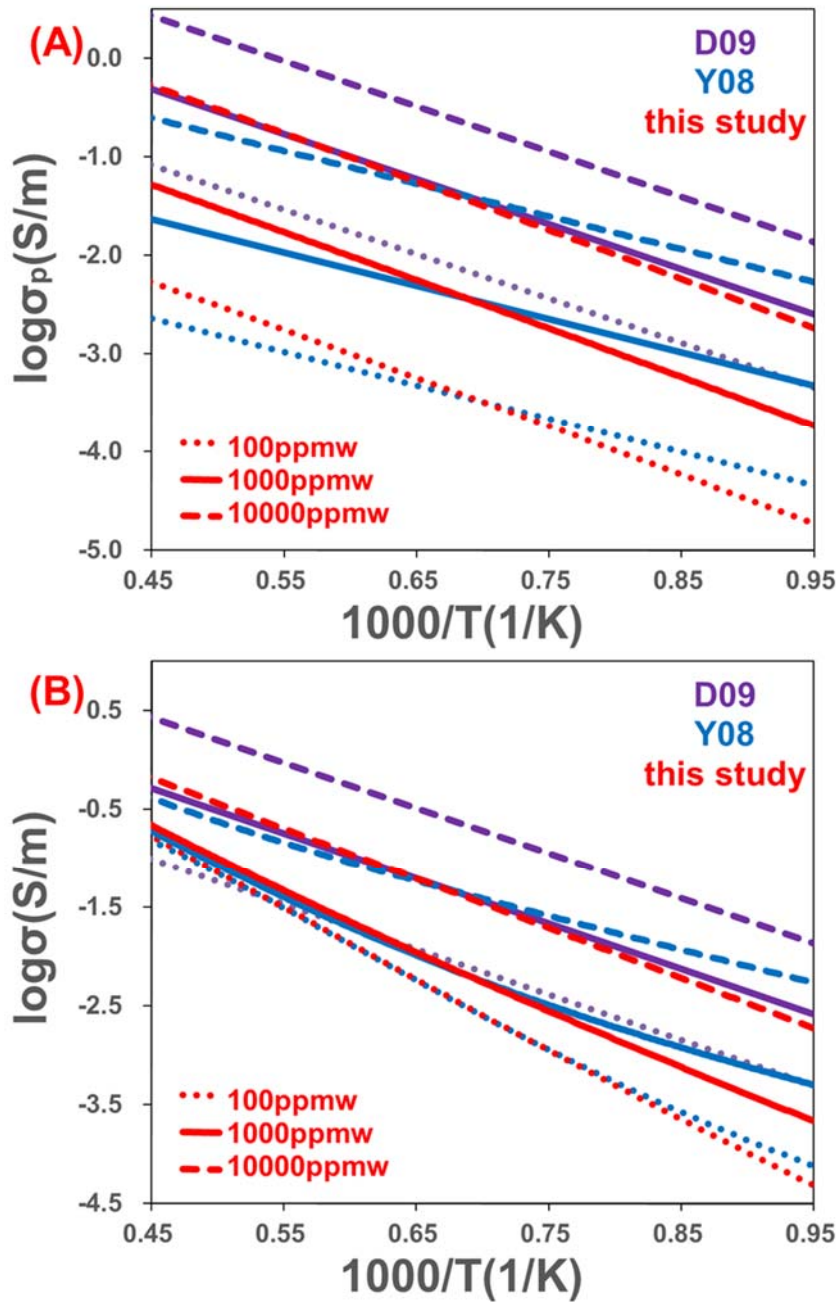


**Fig. 4.10.** (A) and (B) show proton conduction and bulk conductivity considering small polaron conduction mechanisms in Fe-bearing wadsleyite with different water content (100, 1000, 10000 ppmw represented by dotted, solid and dashed line, respectively) as a function of reciprocal temperature, respectively. Y08 and D09 denote data from *Yoshino et al.* [2008] and *Dai et al.* [2009], which showed by purple and blue line, respectively, while red line denotes the calculated conductivities from this study. Small polaron conduction was applied from results of dry Fe-bearing wadsleyite [*Yoshino et al.*, 2008].

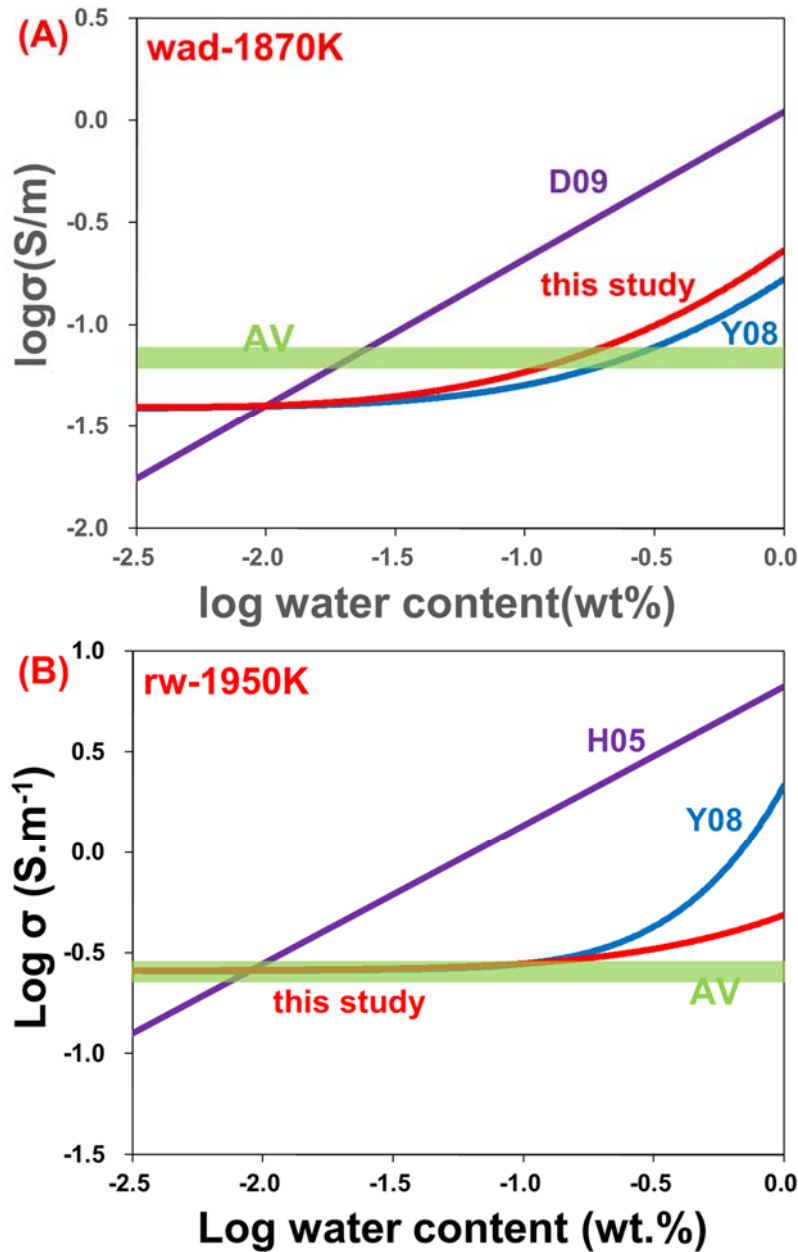


**Fig. 4.11.** Electrical conductivity as a function of water content of (A) Fe-bearing wadsleyite at 1870 K, average geothermal temperature in the upper part of the transition zone [Katsura *et al.*, 2010] and (B) Fe-bearing ringwoodite at 1950 K, average geothermal temperature in the lower part of the transition zone [Katsura *et al.*, 2010]. For Y08 (blue lines) and S15 (red lines) we calculated using fitting parameter from Yoshino *et al.* [2008] and this study, respectively. The purple points are experimental data from Dai *et al.* [2009] and Huang *et al.* [2005] for wadsleyite and ringwoodite, respectively. The green region and AV denote a range of conductivity values observed in the global average model by Kelbert *et al.* [2009]

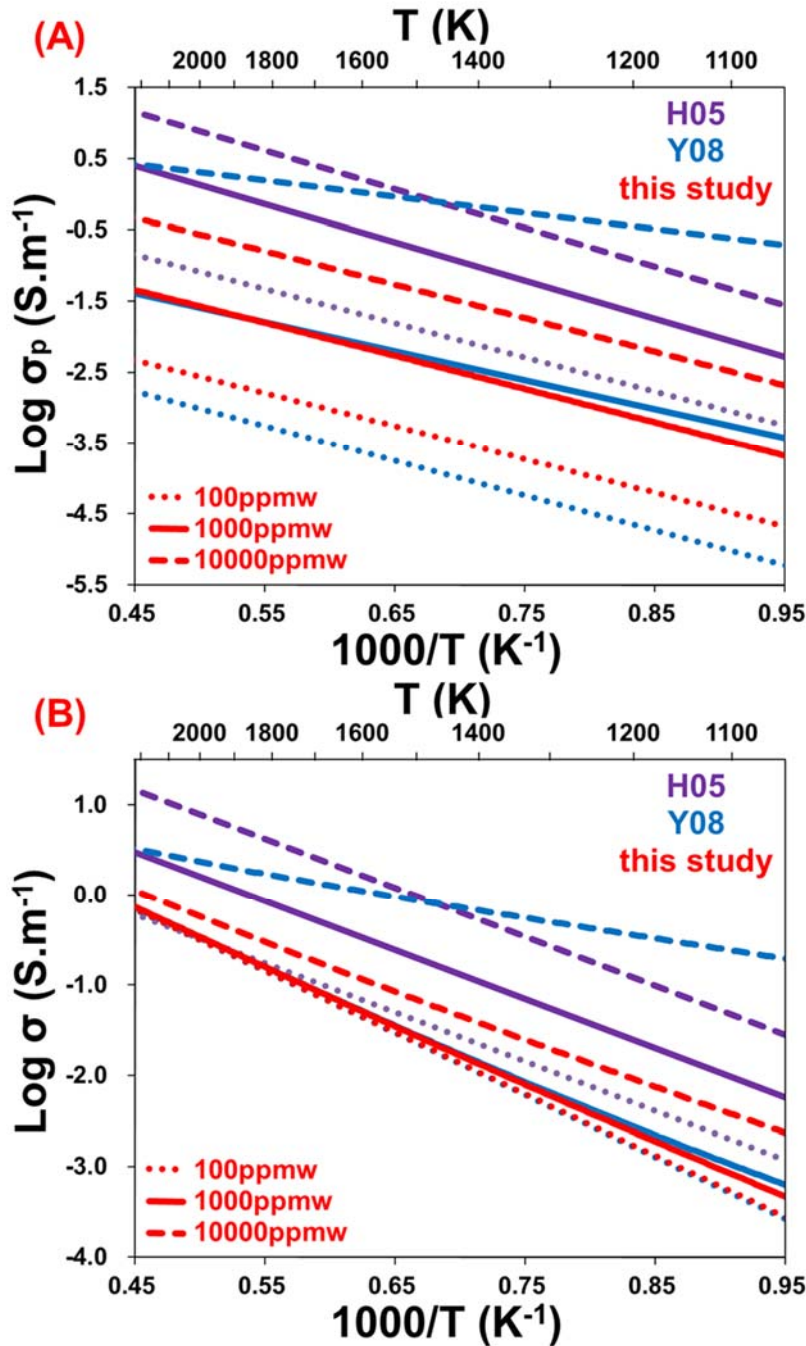


**Fig. 4.12.** (A) and (B) show proton conduction and bulk conductivity considering small polaron conduction mechanisms in Fe-bearing ringwoodite with different water content (100, 1000, 10000 ppmw represented by dotted, solid and dashed line, respectively) as a function of reciprocal temperature, respectively. H05 and Y08 denote data from *Huang et al.* [2005] and *Yoshino et al.* [2008], which showed by purple and blue line, respectively, while red line denotes the calculated conductivities from this study. Small polaron conduction was applied from results of dry Fe-bearing ringwoodite [*Yoshino et al.*, 2008].

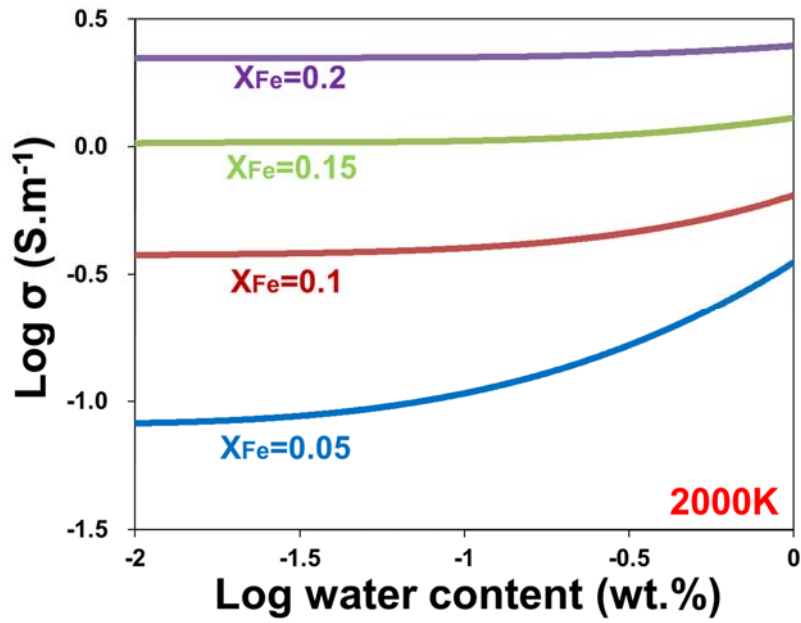


**Fig. 4.13.** Electrical conductivities of Fe-bearing ringwoodite as a function of total iron content for different water contents at 2000K. Hopping conduction in ringwoodite varied with Fe content introduced from *Yoshino et al.* [2009]. Proton conductivities are calculated from hydrogen self-diffusivities in Fe-bearing ringwoodite of this study.

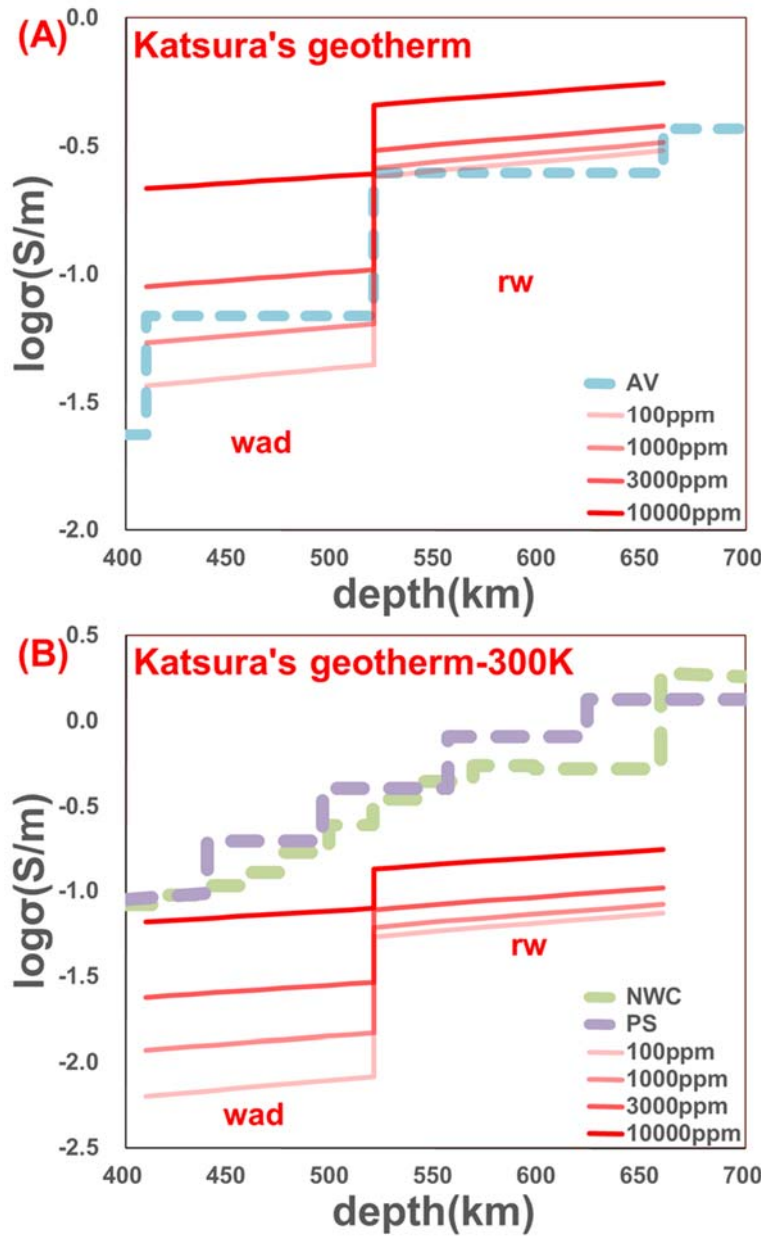


**Fig. 4.14.** Compilation of expected electrical conductivities of Fe-bearing wadsleyite and ringwoodite from hydrogen self-diffusion coefficients as a function of water content. **(A)** Profiles with various water contents showed as red lines are constructed based on the mantle geotherm from *Katsura et al.* [2010]. The blue dashed line denotes a range of conductivity values observed in the global average model by *Kelbert et al.* [2009]. **(B)** Profiles with various water contents showed as red lines are constructed based on 300 K lower than the mantle geotherm from *Katsura et al.* [2010]. Because seismic tomography studies have suggested low-temperature anomalies of 200–300 K associated with subduction slabs beneath the Philippine Sea [*Fukao et al.*, 2004], the conductivity-depth profiles were calculated assuming the

average geotherm [*Katsura et al.*, 2010] minus 300 K. The green and purple dashed lines denote ranges of conductivity values observed by the Magnetotelluric technique beneath northwestern China [*Ichiki et al.*, 2006] and the Philippine Sea [*Baba et al.*, 2010], respectively.

## **Chapter 5**

### **Concluding remarks**

Knowledge of absolute water content in the Earth's mantle is important to understand the mantle dynamics because water strongly influences many physicochemical properties such as melting temperature, seismic velocity, viscosity and electrical conductivity of mantle rocks. In the mantle transition zone, it is well known that the main constituent minerals such as wadsleyite and ringwoodite can store the significant amount of water in their crystal structure based on the large numbers of water solubility experiments. Therefore, the mantle transition zone could be a potential water reservoir of the Earth. To understand role of the mantle transition zone as the water budget, we have to know the absolute water content in this region. Electrical conductivity is believed to be a useful physical parameter to determine the absolute water content in combination between electromagnetic observation and laboratory conductivity measurement. However, laboratory electrical conductivity measurements of proton conduction in nominally anhydrous minerals have provided the large discrepancies because of the experimental difficulty, especially dehydration during the conductivity measurement is unavoidable at high temperatures. To overcome this problem, the other approach to determine electrical conductivity is needed.

In this study, H-D inter-diffusion experiments have been performed in order to determine the hydrogen lattice self-diffusion coefficients in wadsleyite and ringwoodite, which are thought to be a main constituent mineral in the mantle

transition zone, at high pressures and various temperatures in Kawai-type multianvil apparatus. Large single crystals of H- and D-doped wadsleyite and ringwoodite synthesized at 16 and 21 GPa by slow cooling method, respectively, were employed as inter-diffusion couples. As for wadsleyite, single crystals with various Fe contents were prepared to constrain the effect of Fe on the inter-diffusion. Diffusion experiments were also conducted at the same pressures as synthesis and various temperatures ranging from 1000 to 1300 K in Au capsules. Inter-diffusion profiles were measured by secondary ion mass spectroscopy (SIMS). Symmetric diffusion profiles were obtained from diffusion couple of Fe-bearing wadsleyite and ringwoodite. 1-D solutions to Fick's second law indicate that hydrogen diffusivities in Fe-bearing wadsleyite and ringwoodite are nearly the same and about 1 order of magnitude higher than that of olivine determined at 2 GPa from *Du Frane and Tyburczy* [2012]. On the other hand, inter-diffusion profiles obtained from the Fe-free wadsleyite crystal pairs are characterized by much slower diffusion rate and asymmetric diffusion profiles. The model calculation suggests that the dominant hydrogen migration mechanism changes from Mg sites at high ferric concentration condition to interstitial sites with increasing Fe content, and jump probabilities from Mg sites to interstitial sites between deuterium and hydrogen are different.

It has been shown that the present H-D inter-diffusion experimental technique using single crystal pair is capable of determining hydrogen lattice self-diffusion coefficient controlling proton conduction with high accuracy. This method allows distinguishing not only between grain boundary and lattice processes but also between

incorporation and self-diffusion in crystal. Electrical conductivities based on the Nernst-Einstein equation from present hydrogen self-diffusivities in Fe-bearing wadsleyite and ringwoodite are consistent well with those of *Yoshino et al.* [2008] under the transition zone pressure-temperature condition except for ringwoodite with high water content but about 1-2 orders of magnitude lower than *Dai et al.* [2009] and *Huang et al.* [2005]. The discrepancies between direct conductivity measurements and this study were probably caused by various degrees of dehydration during heating in the conductivity measurements. Estimated global average water concentration in the mantle transition zone is less than 0.1 wt.%. In the mantle transition zone beneath the northwestern China, only hydration of wadsleyite and ringwoodite cannot account for both high conductivity and fast seismic velocity anomalies. The characteristic distance for hydrogen diffusion in Fe-bearing wadsleyite is found to be ~1.8 km after 100 Myr. It implies that the heterogeneity of water distribution in the mantle transition zone detected by geophysics observations can be maintained for geologically long time scale. Generation of the supercritical fluid at the top of subducted stagnant slab by heating from the surrounding mantle could be the most plausible explanation for both high conductivity and fast seismic velocity anomalies in the wedge mantle.

## **Acknowledgements**

First of all, I would like to own my best gratitude to my supervisor, Prof. Takashi Yoshino, who patiently and graciously guides, encourages and supports my work and life during the Ph.D period. His really scientist intuition and great perseverance in experiments inspires my growth and expands my horizon in the Earth scientific research.

I also thank Yamazaki sensei, Yoneda sensei, Ito sensei and Tsujino san for their huge help in experimental skills and simulation technique.

I am grateful to Sakamoto sensei and Yurimoto sensei at Hokkaido University for humane help in SIMS determinations, Yamasita sensei for selfless help in FTIR measurements and Yachi san for kind help in EMPA measurements.

It is my honor to have nice days together with many Chinese friends including Fang Xu, Xinzhuan Guo, Shuangming Shan, Riping Wang, Baohua, Zhang, Fei Hongzhan and Longjian Xie in the past at Misasa.

Finally, Thank all the colleagues and technicians in the Institute for our life, study and education. I will never forget this happy memory at Misasa forever.

## References

- Baba, K., H. Utada, T. Goto, T. Kasaya, H. Shimizu and N. Tada (2010), Electrical conductivity imaging of the Philippine Sea upper mantle using seafloor magnetotelluric data, *Phys. Earth Planet. Inter.*, 183, 44-62.
- Balluffi, R.W., S.M. Allen and W.C. Carter (2005), Kinetics of Materials, *Wiley-Interscience, Hoboken*, 645.
- Banks, J.R. and P. Ottey (2007), Geomagnetic Deep Sounding in and around the Kenya Rift Valley, *Geophys. J. Int.*, 36, 321-335.
- Bell, D.R. and P.D. Ihinger (2000), The isotopic composition of hydrogen in nominally anhydrous mantle minerals, *Geochim. Cosmochim. Acta* 64, 2109–2118.
- Bell, D.R., G.R. Rossman, J. Maldener, D. Endisch, and F. Rauch (2003), Hydroxide in olivine: A quantitative determination of the absolute amount and calibration of the IR spectrum, *J. Geophys. Res.*, 108, 2105B2.
- Bolfan-Casanova, N., H. Keppler and D.C. Rubie (2000), Water partitioning between nominally anhydrous minerals in the MgO-SiO<sub>2</sub>-H<sub>2</sub>O system up to 24 GPa: implications for the distribution of water in the Earth's mantle, *Earth Planet. Sci. Lett.*, 182, 209–221.
- Booker, J.R., A. Favetto and M.C. Pomposiello (2004), Low electrical resistivity associated with plunging of the Nazca flat slab beneath Argentina, *Nature*, 429, 399–403.

- Carslaw, H.S. and J.C. Jaeger (1959), *Conduction of Heat in Solids*, Clarendon, Oxford, press.
- Crank, J. (1979), *The Mathematics of Diffusion*, Oxford Univ. Press.
- Dai, L. and S. Karato (2009), Electrical conductivity of wadsleyite at high pressures and high temperatures, *Earth Planet. Sci. Lett.*, 287, 277–83.
- Dai, L. and S. Karato (2014), High and highly anisotropic electrical conductivity of the asthenosphere due to hydrogen diffusion in olivine, *Earth Planet. Sci. Lett.*, 408, 79–86.
- Demouchy, S. (2010), Diffusion of hydrogen in olivine grain boundaries and implications for the survival of water-rich zones in the Earth's mantle, *Earth Planet. Sci. Lett.*, 295, 305–13.
- Demouchy, S. and S.J. Mackwell (2003), Water diffusion in synthetic iron-free forsterite, *Phys Chem Miner.*, 30, 486–494.
- Demouchy, S. and S.J. Mackwell (2006), Mechanisms of hydrogen incorporation and diffusion in iron-bearing olivine, *Phys Chem Miner.*, 33, 347–355.
- Demouchy, S., E. Deloule, D.J. Frost and H. Keppler (2005), Pressure and temperature-dependence of water solubility in Fe-free wadsleyite, *Am. Mineral.*, 90, 1084–91.
- Du Frane, W.L. and J.A. Tyburczy (2012), Deuterium-hydrogen exchange in olivine: implications for point defects and electrical conductivity, *Geochem. Geophys. Geosyst.*, 13, Q03004.
- Egbert, G.D. (2007), Robust multiple-station magnetotelluric data processing,

*Geophys. J. Int.*, 130, 475-496.

Evans, R.L., G. Hirth, K. Baba, D. Forsyth, A. Chave and R. Mackie (2005), Geophysical evidence from the MELT area for compositional controls on oceanic plates, *Nature*, 437, 249–52.

Fukao Y., T. Koyama, M. Obayashi and H. Utada (2004), Trans-Pacific temperature field in the mantle transition region derived from seismic and electromagnetic tomography, *Earth Planet. Sci. Lett.*, 217, 425-34.

Gudmundsson, G. and B.J. Wood (1995), Experimental tests of garnet peridotite oxygen barometry, *Contrib. Mineral. Petrol.* 119, 56–67.

Hae, R., E. Ohtani, T. Kube, T. Koyama and H. Utada (2006), Hydrogen diffusivity in wadsleyite and water distribution in the mantle transition zone, *Earth Planet. Sci. Lett.*, 243(1-2), 141-148.

Hiraga, T. and D.L. Kohlstedt (2007), Equilibrium interface segregation in the diopside–forsterite system I: analytical techniques, thermodynamics, and segregation characteristics, *Geochim. Cosmochim. Acta*, 71, 1266–1280.

Hiraga, T. and D.L. Kohlstedt (2009), Systematic distribution of incompatible elements in mantle peridotite: importance of intra- and inter-granular melt-like component, *Contrib. Mineral. Petrol.*, 158, 149–167.

Holl, M., J.R. Smyth, S.D. Jacobsen and D. Frost (2008), Effects of hydration on the structure and compressibility of wadsleyite, beta-(Mg<sub>2</sub>SiO<sub>4</sub>). *Am. Mineral.* 93, 598–607.

Huang, X., Y. Xu and S. Karato (2005), Water content in the transition zone from

- electrical conductivity of wadsleyite and ringwoodite, *Nature*, 434, 746-49.
- Ichiki, M., K. Baba, M. Obayashi, H. Utada (2006), Water content and geotherm in the upper mantle above the stagnant slab: interpretation of electrical conductivity and seismic P-wave velocity models, *Phys. Earth Planet. Inter.*, 155, 1-15.
- Ichiki, M., M. Uyeshima, H. Utada, G. Zhao, J. Tang and M. Ma (2001), Upper mantle conductivity structure of the back-arc region beneath northeastern China. *Geophys. Res. Lett.*, 28, 3773–76.
- Inoue, T., D.J. Weidner, P. A. Northrup, and J.B. Parise (1998), Elastic properties of hydrous ringwoodite (gamma-phase) in Mg<sub>2</sub>SiO<sub>4</sub>, *Earth Planet. Sci. Lett.* 160, 107-113.
- Inoue, T., H. Yurimoto and Y. Kudoh (1995), Hydrous modified spinel, Mg<sub>1.75</sub>SiH<sub>0.5</sub>O<sub>4</sub>: a new water reservoir in the mantle transition region, *Geophys. Res. Lett.*, 22, 117–120.
- Ito, E. and H. Sato (1991), Aseismicity in the lower mantle by superplasticity of the descending slab, *Nature*, 351.
- Jacobsen, S.D., S. Demouchy, D.J. Frost, T. Boffa-Ballaran and J. Kun (2005), A systematic study of OH in hydrous wadsleyite from polarized FTIR spectroscopy and single-crystal X-ray diffraction: Oxygen sites for hydrogen storage in Earth's interior, *Am. Mineral.*, 90, 61–70.
- Jones, A.G., J. Fullea, R.L. Evans and M.R. Muller (2012), Water in cratonic lithosphere: calibrating laboratory determined models of electrical

- conductivity of mantle minerals using geophysical and petrological observations, *Geochem. Geophys. Geosyst.*, *13*, Q06010.
- Karato, S. (1990), The role of hydrogen in the electrical conductivity of the upper mantle, *Nature*, *347*, 272-73.
- Karato, S. (2008), *Deformation of earth materials: an introduction to the rheology of solid earth*, Cambridge Univ. Press.
- Karato, S. (2011), Water distribution across the mantle transition zone and its implications for global material circulation, *Earth Planet. Sci. Lett.*, *301*, 413–23.
- Karato, S. (2013), Theory of isotope diffusion in a material with multiple species and its implications for hydrogen-enhanced electrical conductivity in olivine, *Phys. Earth Planet. Inter.*, *219*, 49-54.
- Katsua, T., A. Yoneda, D. Yamazaki, T. Yoshino and E. Ito (2010), Adiabatic temperature profile in the mantle, *Phys. Earth Planet. Inter.*, *183*, 212-18.
- Katsura, T., K. Sato and E. Ito (1998), Electrical conductivity of silicate perovskite at lower-mantle conditions. *Nature*, *395*, 493–95.
- Kelbet A., A. Schultz and G. Egbert (2009), Global electromagnetic induction constraints on transition-zone water content variations, *Nature*, *460*, 1003-1006.
- Keppler, H. and J.R. Smyth (2006), Water in Nominally Anhydrous Minerals, *Rev Mineral Geochem.*, *62*, 1-478.
- Khan, A. and T.J. Shankland (2012), A geophysical perspective on mantle water

- content and melting: inverting electromagnetic sounding data using laboratory-based electrical conductivity profiles, *Earth Planet. Sci. Lett.*, 317–18, 27–43.
- Kohlstedt, D.L., H. Keppeler and D.C. Rubie (1996), Solubility of water in the  $\alpha$ ,  $\beta$  and  $\gamma$  phases of  $(\text{Mg, Fe})_2\text{SiO}_4$ , *Contributions to Mineralogy and Petrology*, 123, 345–357.
- Kohlstedt, D.L. and S.J. Mackwell (1998), Diffusion of hydrogen and intrinsic point defects in olivine, *Zeitschrift für Physikalische Chemie*, 207, 147–162.
- Kröger, F.A. and H.J. Vink, 1956. Relation Between the Concentrations of Imperfections in Crystalline Solids. *Academy Press, New York*.
- Kuvshinov, A., H. Utada, D. Avdeev and T. Koyama (2005), 3-D modelling and analysis of Dst C-responses in the North Pacific Ocean region, revisited, *Geophys. J. Int.*, 160, 505–26.
- Li, Y., R. Dasgupta and K. Tsuno (2015), The effects of sulfur, silicon, water, and oxygen fugacity on carbon solubility and partitioning in Fe-rich alloy and silicate melt systems at 3 GPa and 1600 °C: Implications for core–mantle differentiation and degassing of magma oceans and reduced planetary mantles. *Earth Planet. Sci. Lett.* 415, 54–66.
- Litaso, K.D. and E. Ohtani (2009), Solidus and phase relations of carbonated peridotite in the system  $\text{CaO-Al}_2\text{O}_3\text{-MgO-SiO}_2\text{-Na}_2\text{O-CO}_2$  to the lower mantle depths, *Phys. Earth Planet. Inter.*, 177, 46–58.
- Litasov, K., A. Shatzkiy, E. Ohtani and T. Katsura (2011), Systematic study of

- hydrogen incorporation into Fe-free wadsleyite, *Phys. Chem. Mineral.*, *38*, 75–84.
- Liu, L. (2002), Are hydrous phases more compressible? Implications for high-velocity zones in the deep mantle. *Geophys. J. Int.* *149*, 37–43.
- Lizarralde, D., A.D. Chave, G. Hirth and A. Schultz (1995), A Northern Pacific mantle conductivity profile from long-period magnetotelluric sounding using Hawaii-to-California submarine cable data, *J. Geophys. Res.*, *100*, 17837–54.
- Mackwell, S., M. Bystricky and C. Sproni (2004), Fe-Mg interdiffusion in (Mg,Fe)O, *Phys. Chem. Mineral.*, *32*, 418–425.
- Manthlaka, G., T. Matsuzaki, T. Yoshino, S. Yamashita, E. Ito and T. Katsura (2009), Electrical conductivity of wadsleyite as a function of temperature and water content, *Phys. Earth Planet. Inter.*, *174*, 10–18.
- Mao, Z., J.F. Lin, D.J. Steven, S.D. Thomas, Y.Y. Chang, J.R. Smyth, D.J. Frost, H.E. Hauri and V.B. Prakapenka (2012), Sound velocities of hydrous ringwoodite to 16 GPa and 673 K, *Earth Planet. Sci. Lett.*, *331–332*, 112–119.
- McCammon, C.A., D.J. Frost, J.R. Smyth, H.M.S. Laustsen, T. Kawamoto, N.L. Ross and P.A. van Aken (2004), Oxidation state of iron in hydrous mantle phases: implications for subduction and mantle oxygen fugacity, *Phys. Earth Planet. Inter.*, *143–144*, 157–169.
- Melekhova, E., M.W. Schmidt, P. Ulmer and T. Pettke (2007), The composition of liquids coexisting with dense hydrous magnesium silicates at 11–13.5 GPa and the endpoints of the solidi in the MgO–SiO<sub>2</sub>–H<sub>2</sub>O system, *Geochim.*

*Cosmochim. Acta*, 71, 3348–3360.

Mitchell, A.C. and W.J. Nellis (1982), Equation of state and electrical conductivity of water and ammonia shocked to the 100 GPa (1 Mbar) pressure range, *J. Chem. Phys.*, 76, 6273–6281.

Neal, S.L., R.L. Mackie, J.C. Larsen and A. Schultz (2000), Variations in the electrical conductivity of the upper mantle beneath North America and the Pacific Ocean, *J. Geophys. Res.*, 105, 8229–42.

Nishihara, Y., T. Shinmei and S. Karato (2006), Grain-growth kinetics in wadsleyite: Effects of chemical environment, *Phys. Earth Planet. Inter.*, 154, 30–43.

Olsen, N. (1998), The electrical conductivity of the mantle beneath Europe derived from C-responses from 3 to 270 hours, *Geophys. J. Int.*, 133, 298–308.

Ohtani, E., K. Litasov, T. Hosoya, T. Kubo and T. Kondo (2004), Water transport into the deep mantle and formation of a hydrous transition zone. *Phys. Earth Planet. Inter.*, 143-144, 255-269.

Ohtani, E., T. Kubo, T. Kondo and T. Kikegawa (2003), In situ X-ray observation of decomposition of superhydrous phase B at high pressure and temperature, *Geophys. Res. Lett.*, 30, 1-4.

O'Neill, H.S.C., D.C. Rubie, D. Canil, C.A. Geiger, C.R. Ross, II, F. Seifert and A.B. Woodland (1993), Ferric iron in the upper mantle and in transition zone assemblages: implications for relative oxygen fugacities in the mantle. In: Takahashi, T., Jeanloz, R., Rubie, D.C. (Eds.), *Evolution of the Earth and Planets. American Geophysical Union, Washington, DC*, 73–88.

- PadrónNavartaa, J.A., J. Hermann and H.S.C. O'Neill (2014), Site-specific hydrogen diffusion rates in forsterite, *Earth Planet. Sci. Lett.*, *392*, 100-112.
- Paterson, M. S. (1982), The determination of hydroxyl by infrared absorption in quartz, silicate glasses, and similar materials, *Bull. Mineral.*, *105*, 20–29.
- Pearson D. G., F. E. Brenker, F. Nestola, J. McNeill, L. Nasdala, M. T. Hutchison, S. Matveev, K. Mather, G. Silversmit, S. Schmitz, B. Vekemans and L. Vincze (2014), Hydrous mantle transition zone indicated by ringwoodite included within diamond, *Nature* *507*, 221–224.
- Petry, C. (1999), Experimente zur Ni-Diffusion in Olivin, Kalibration des Ni-Fe / Metall-Olivin-Austauschthermometers und deren Anwendung in der Kosmochemie, *PhD thesis, University of Cologne*.
- Riedel, M. and S. Karato (1997), Grain-size evolution in subducted oceanic lithosphere associated with the olivine–spinel transformation and its influence on rheology, *Phys. Earth Planet. Inter.*, *148*, 27-43.
- Ringwood, A. E. (1962), A Model for the upper mantle, *J. Geophys. Res.*, *67*, 857-867.
- Ringwoodite, A.E. and A. Major (1970), The system  $Mg_2SiO_4 - Fe_2SiO_4$  at high pressure and temperatures, *Phys. Earth Planet. Inter.*, *3*, 89–108.
- Romano, C., B.T. Poe, J. Tyburczy and F. Nestra (2009), Electrical conductivity of hydrous wadsleyite, *Eur. J. Mineral.*, *21*, 615–22.
- Rubie, D. and A. Brearley (1990), Mechanism of the  $\gamma$ - $\beta$  phase transformation of  $Mg_2SiO_4$  at high temperature and pressure, *Nature*, *348*, 628-631.

- Sano-Furukawa, A., T. Kuribayashi, K. Komatsu, T. Yagi and E. Ohtani (2011), Investigation of hydrogen sites of wadsleyite: A neutron diffraction study, *Phys. Earth Planet. Inter.*, 189, 56–62.
- Seama, N., K. Baba, H. Utada, H. Toh H and N. Tada (2007), 1-D electrical conductivity structure beneath the Philippine Sea: results from an ocean bottom magnetotelluric survey, *Phys. Earth Planet. Inter.*, 162, 2–12.
- Semenov, V.Y. and W. Jozwiak (2006), Lateral variations of the mid-mantle conductance beneath Europe, *Tectonophysics*, 416, 279–88.
- Schultz, A., R.D. Kurtz, A.D. Chave and A.G. Jones (1993), Conductivity discontinuities in the upper mantle beneath a stable craton, *Geophys. Res. Lett.*, 20, 2941–44.
- Shatsky, A., K.D. Litasov, T. Matsuzaki, K. Shinoda, D. Yamazaki, A. Yoneda, E. Ito and T. Katsura (2009), Single crystal growth of wadsleyite, *Am. Mineral.*, 94, 1130-1136.
- Shatsky, A., D. Yamazaki, Y.M. Borzdov, T. Matsuzaki, K.D. Litasov, T. Cooray, A. Ferot, E. Ito and T. Katsura (2010), Stishovite single-crystal growth and application to silicon self-diffusion measurements, *Am. Mineral.*, 95, 135-143.
- Shekhar, S. (2012), The origins of olivine fabric transitions and their effects on seismic anisotropy in the upper mantle, *Ph.D thesis, University of Bayreuth*.
- Shewmon, P. (1989), Diffusion in Solids, *The Minerals, Metals & Materials Society, Warrendale, Pennsylvania*.
- Shimizu, H., T. Koyama, H. Baba and H. Utada (2010), Revised 1-D mantle electrical

- conductivity structure beneath the north Pacific, *Geophys. J. Int.*, *180*, 1030–48.
- Shimojuku, A., T. Kubo, E. Ohtani, T. Nakamura, R. Okazaki, R. Dohmen and S. Chakraborty (2009), Si and O diffusion in (Mg,Fe)<sub>2</sub>SiO<sub>4</sub> wadsleyite and ringwoodite and its implications for the rheology of the mantle transition zone, *Earth Planet. Sci. Lett.*, *284*, 103-112.
- Smyth, J.R. (1994), A crystallographic model for hydrous wadsleyite ( $\beta$ -Mg<sub>2</sub>SiO<sub>4</sub>): an ocean in the Earth's interior? *Am. Mineral.* *79*, 1021–1024.
- Tarits, P., S. Hautot and F. Perrier (2004), Water in the mantle: results from electrical conductivity beneath the French Alps, *Geophys. Res. Lett.*, *31*, L06612
- Utada, H., T. Koyama, H. Shimizu and A.D. Chave (2003), A semi-global reference model for electrical conductivity in the mid-mantle beneath the north Pacific region, *Geophys. Res. Lett.*, *30*, 1194.
- Verma, A.K. and B.B. Karki (2009), Ab initio investigations of native and protonic point defects in Mg<sub>2</sub>SiO<sub>4</sub> polymorphs under high pressure, *Earth Planet. Sci. Lett.*, *285*, 140-149.
- Wang, D., M. Mookherjee, Y. Xu and S. Karato (2006), The effect of water on the electrical conductivity of olivine, *Nature* *443*, 977-980.
- Xu, Y., B.T. Poe, T.J. Shankland and D.C. Rubie (1998), Electrical conductivity of olivine, wadsleyite, and ringwoodite under upper-mantle conditions. *Science*, *280*, 1415–18.
- Xu, Y., T.J. Shankland, S. Linhardt, D.C. Rubie, F. Langenhorst and K.

- Klasinski (2004), Thermal diffusivity and conductivity of olivine, wadsleyite and ringwoodite to 20 GPa and 1373 K. *Phys. Earth Planet. Inter.*, 143-144, 321-336.
- Yoshio, T. (2010), Laboratory Electrical Conductivity Measurement of Mantle Minerals, *Surv Geophys.*, 31, 163–206.
- Yoshin, T. and T. Katsura (2009), Effect of iron content on electrical conductivity of ringwoodite, with implications for electrical structure in the mantle transition zone, *Phys. Earth Planet. Inter.*, 174, 3-9.
- Yoshio, T. and T. Katsura (2012), Re-evaluation of electrical conductivity of anhydrous and hydrous wadsleyite, *Earth Planet. Sci. Lett.*, 337-338, 56-67.
- Yoshino, T. and T. Katsura (2013), Electrical Conductivity of Mantle Minerals: Role of Water in Conductivity Anomalies, *Annu. Rev. Earth Planet. Sci.*, 2013, 41, 605-628.
- Yoshino, T., G. Manthilake, T. Matsuzaki and T. Katsura (2008), Dry mantle transition zone inferred from electrical conductivity of wadsleyite and ringwoodite, *Nature*, 451, 326-29.
- Yoshio, T., T. Matsuzaki, S. Yamashita and T. Katsura (2006), Hydrous olivine unable to account for conductivity anomaly at the top of the asthenosphere, *Nature* 443, 973-976.
- Yoshino, T., T. Yosuko, D.A. Wark and E.B. Watson (2005), Grain boundary wetness of texturally equilibrated rocks, with implications for seismic properties of the mantle, *J. Geophys. Res.*, 110, B08205.